

Chapter 2

The Earth Atmosphere and Space

The Earth's atmosphere has always acted as a screen between the observer and the rest of the Universe. The pre-Copernicans regarded it as the seat of the volatile elements because of its mobility, separating as it did the sublunar world from the world of the stars. From the time of Galileo, and up until the conquest of space, observations of photons were limited to the narrow window of the visible, and this range was extended only recently by the addition of radio frequencies.¹ Despite the recent development of observation from space, ground-based observation retains considerable advantages in terms of both access and cost. The global strategy of observational astronomy therefore requires an exact knowledge of the properties of the Earth's atmosphere. With such a knowledge, the potential or the limits of ground-based observation can be defined, and, for each wavelength of the spectrum, the best altitude can be determined and the best sites chosen for new instruments. The choice of site is crucial. Many factors must be taken into account, and we shall describe them here. The Antarctic continent is now accessible for astronomy and will no doubt provide many important opportunities.

In this chapter, we examine one by one the physical properties and composition of the atmosphere, which lead to its *opacity*, that is, to its capacity to absorb radiation. *Atmospheric scattering* prevents daytime observation in the visible, and causes light pollution at night. *Refraction* and *dispersion* deviate the apparent direction of a star chromatically, i.e., in a wavelength-dependent way, from its true direction. The *thermal emission* of the atmosphere perturbs infrared and millimetre observation during both the day and the night. *Atmospheric turbulence* degrades images and causes phase fluctuations which affect the working of telescopes and interferometers. *Ionisation* of the upper atmosphere creates a plasma which modifies the propagation of radio waves. Furthermore, all these phenomena vary with time and, for the most part, are strongly dependent on geographical location.

¹The first radioastronomical observation was made by American astronomer Karl Jansky (1905–1950), who observed the Sun in 1933, using a telecommunications antenna.

During the twentieth century, development of observation from space has made the *whole electromagnetic spectrum* available to observation.² However, even in space, there remain parasitic phenomena which perturb observation, in the same way as the atmosphere for Earth-based observation, and it will not be out of place also to tackle these questions in the present chapter, for the sake of completeness.

2.1 Physical and Chemical Structure of the Atmosphere

In this section we discuss the highly variable properties of the Earth atmosphere as a function of altitude. This is important when deciding whether to situate an observatory at sea level, on a mountain top, aboard an aircraft, or in a stratospheric balloon, depending on the properties required for observing the relevant wavelength.

2.1.1 Vertical Structure

To a first approximation, the Earth's atmosphere is in radiative equilibrium with its surroundings. The overall balance, over the whole Earth, of the flux received from the Sun and that which is re-radiated into space leads to a more or less stationary distribution of temperatures, pressures, and so on, with respect to time, although daily, annual, and even secular cycles are superposed.

The average structure of the atmosphere is described as a function of altitude z by temperature and density distributions, $T(z)$ and $\rho(z)$, respectively (Fig. 2.1). Note the *troposphere* ($\partial T/\partial z < 0$, in general), which is separated from the *stratosphere* ($\partial T/\partial z > 0$, in general) by the *tropopause*. The height of the tropopause is strongly dependent on the latitude, almost reaching ground level over the Antarctic continent (altitude of the Southern Polar cap ~ 3.4 km). At all latitudes, significant deviations from the average distribution are observed near ground level. In particular, there are *inversion layers* where the temperature gradient changes sign through a certain vertical distance, which can be more than one kilometre.

From 0 to 90 km, the composition of the air can be considered as constant, and the pressure is approximately described by an exponential law:

$$P(z) = P_0 \exp(-z/H), \quad H = \frac{R}{M_0} \frac{T_m}{g},$$

where H is the scale height, M_0 the mean molecular mass of the air, and T_m a mean temperature. Taking $R = 8.32 \text{ J K}^{-1} \text{ mole}^{-1}$, $M_0 = 0.029 \text{ kg}$, gives the value $H = 7998 \text{ m} \simeq 8 \text{ km}$ near ground level.

²The first balloons equipped with detectors date from about 1910, the first scientific rocket launches from 1946 (using the German V-2 rocket), and the first satellites in orbit from 1960.

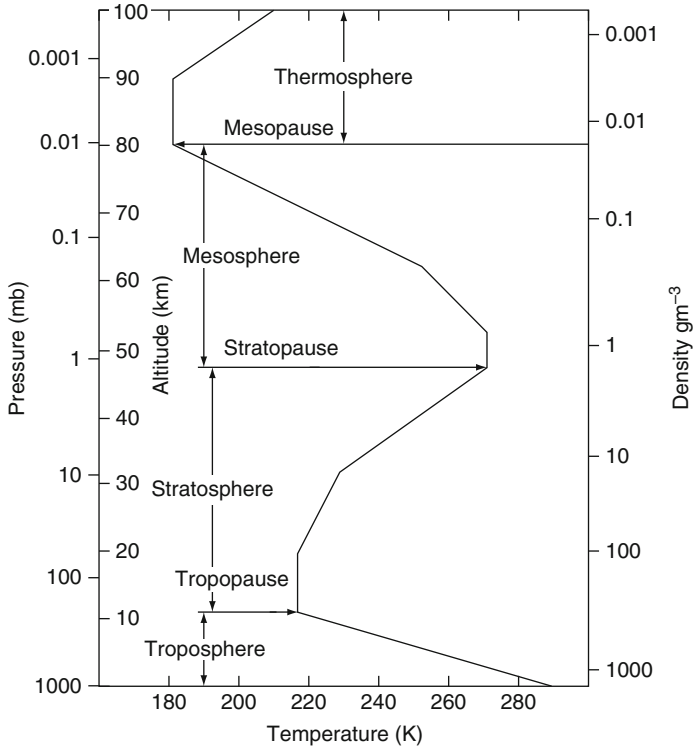


Fig. 2.1 Temperature profile $T(z)$, density $\rho(z)$, and pressure $P(z)$ in the mean atmosphere. The names of the layers and their boundaries are those adopted by the World Meteorological Organisation. (After U.S. Standard Atmosphere)

The adiabatic gradient of dry air has value around 0.01°m^{-1} near ground level, and is given by the formula

$$\left(\frac{\partial T}{\partial z}\right)_{\text{ad}} = -\frac{g}{R}M_0\frac{C_p - C_v}{C_p} \quad (C_p, C_v \text{ specific heats}).$$

Any gradient larger than this in absolute value would imply *convective instability* of the atmosphere, and hence vertical currents.

Space observatories are placed in orbits above 300 km, an altitude at which the residual amount of atmosphere is not totally negligible (Fig. 2.2).

2.1.2 Constituents of the Atmosphere

The principal constituents are O_2 and N_2 , whose relative proportions are constant between 0 and 100 km. Study of the *minor atmospheric constituents* in these layers

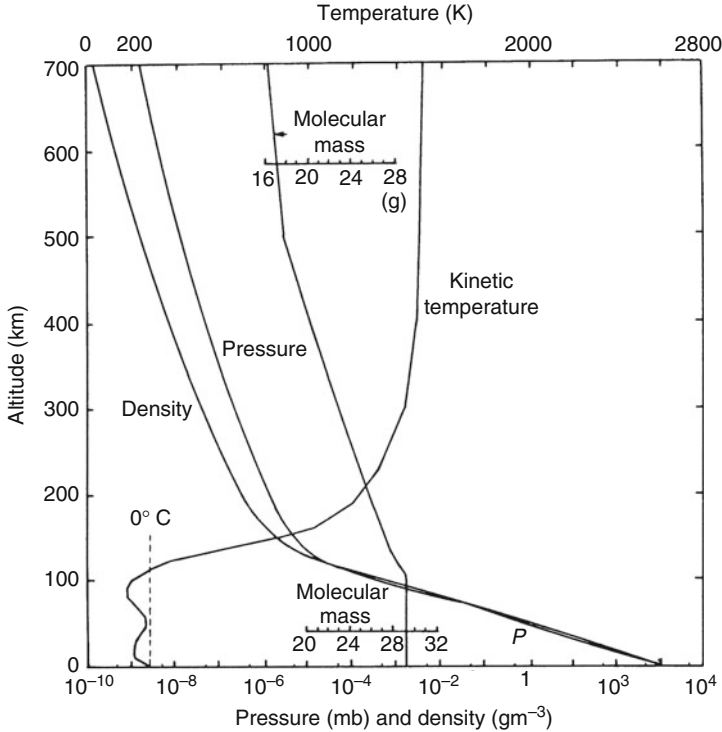


Fig. 2.2 Temperature, density, and molecular mass profiles between 0 and 700 km altitude. There are significant variations with latitude or solar activity in these average profiles. (U.S. Standard Atmosphere)

is an active area of research, considering their role in the maintenance of physical conditions at the Earth's surface (radiative balance, ultraviolet flux), and the possible disturbance of the natural equilibrium by human activity. Some of these constituents also play an important role in astronomical observations, because of the strong absorption they cause in certain spectral bands. In particular, water vapour, carbon dioxide, and ozone can be cited.

Water Vapour

The *mixing ratio* or *fractional content* is defined locally as

$$r = \frac{\text{mass of H}_2\text{O per m}^3}{\text{mass of air per m}^3},$$

which is usually measured in g kg^{-1} . This ratio varies between 0 and a maximum value $r_s(T)$ which is characteristic of saturation, and is also a very rapidly varying

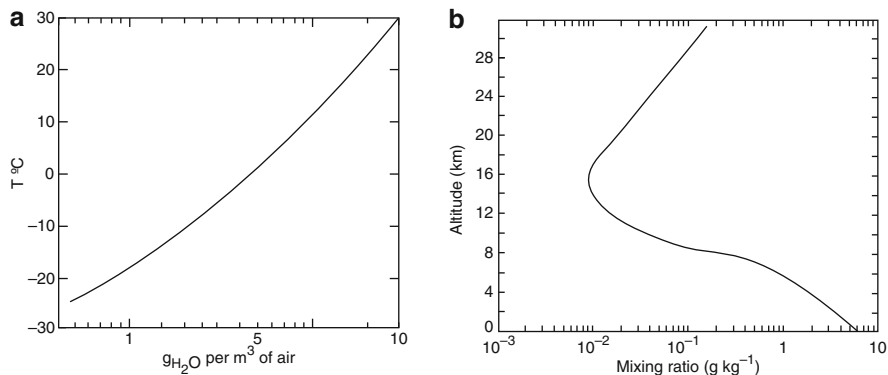


Fig. 2.3 (a) Mass concentration of water vapour in saturated air, at normal pressure, as a function of temperature. (b) Mixing ratio $r(z)$ of water vapour in air as a function of altitude for an average atmosphere. $r(z)$ is measured in $g\ kg^{-1}$, so that it is close to unity for the most frequently encountered meteorological conditions near ground level

function of air temperature (Fig. 2.3a). The mixing ratio is a function of altitude, and is also strongly dependent on both time and latitude (Fig. 2.3b).

The *quantity of precipitable water* above altitude z_0 is defined as

$$w(z_0) = \int_{z_0}^{\infty} N_{H_2O} dz,$$

where $N_{H_2O}(z)$ the number of molecules per unit volume. For normal pressure and temperature P_0 and T_0 , respectively,

$$N_{H_2O} [m^{-3}] = 4.3 \times 10^{25} \frac{P}{P_0} \frac{T}{T_0} r(z).$$

This quantity can also be expressed as a column of precipitable water

$$h_{H_2O} [cm] = \rho_0 [g\ cm^{-3}] \int_{z_0}^{\infty} r(z) e^{-z/H} dz,$$

where ρ_0 is the air density at altitude z_0 , and z is given in centimetres.

Because of the rapid variation of $r(z)$ with height, the scale height of water vapour is considerably less than that of dry air H , being something like 3 km in the troposphere. Thus, siting an observatory on a high mountain, at an altitude of several kilometres, significantly improves the quality of observation, especially in the infrared and at millimetre wavelengths. The Antarctic plateau, at an altitude of around 3 000 m, also provides favourable observing conditions (see Sect. 2.8.6).

Ozone

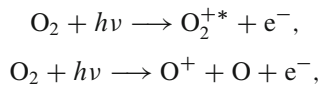
The vertical distribution of ozone depends on the latitude and the season. This layer has been the subject of much interest since the detection of perturbations which may be due to human activity, notably the destructive role of certain industrial products such as fluorocarbons in the 1980s. Referred to normal conditions, the integrated quantity of ozone in the whole atmosphere varies from a column of 0.24 cm to a column of 0.38 cm STP (Standard Temperature and Pressure) in going from low to high altitudes. The maximum concentration occurs at about 16 km, although ozone is present even at 80 km. It absorbs mainly in the ultraviolet ($\lambda \lesssim 300$ nm).

Carbon Dioxide

This constituent is an important source of infrared absorption. Its vertical distribution is similar to those of O_2 and N_2 , and its mixing ratio is independent of altitude. It absorbs mainly in the mid-infrared.

Ions

The atmosphere becomes increasingly ionised above 60 km, because of the Sun's ultraviolet radiation, which cause a series of photochemical reactions of the type



where O_2^{+*} denotes an excited state of O_2 . The inverse reactions of recombination, and of radiative or collisional de-excitation, also occur, in such a way that the electron density is not constant at a given altitude. It varies considerably with altitude and solar illumination (the *circadian* or day–night cycle), as well as with solar activity. Solar flares (see Fig. 6.37) increase the ultraviolet flux, and cause electron showers which are channelled along the Earth's magnetic field lines and which ionise the atmosphere at high latitudes (auroral zones).

Several ionospheric layers are distinguished, corresponding to local maxima of electron density N_e , as shown in Table 2.1. Beyond these layers, the level of ionisation remains effectively constant up to about 2 000 km, with $N_e \sim 10^4 \text{ cm}^{-3}$.

Table 2.1 Ionospheric layers

Layer	Altitude [km]	Electron density N_e [cm^{-3}]
<i>D</i>	60	10^3
<i>E</i>	100	10^5
<i>F</i>	150–300	2×10^6

2.2 Absorption of Radiation

Absorption of radiation by the constituents of the atmosphere can be either total or partial. If it is total, *transmission windows* can be defined at a given altitude, and the minimum altitude at which an observation becomes possible can be determined. If it is partial, it will modify the spectra of the sources under observation; these spectra will be affected by *telluric absorption bands*, whose position, intensity, and equivalent width must be identified (see Sect. 8.1).

Atomic and Molecular Transitions

These transitions cause absorption at discrete wavelengths. The types of transition are:

- *pure rotational* molecular transitions, e.g., H₂O, CO₂, O₃,
- *rotational–vibrational* molecular transitions, e.g., CO₂, NO, CO,
- *electronic* molecular transitions, e.g., CH₄, CO, H₂O, O₂, O₃, or radicals such as OH,
- *electronic* atomic transitions, e.g., O, N.

Atomic and molecular physics allow calculation of the *absorption coefficients* $\kappa_i(\lambda)$ (with units cm² g⁻¹) and *cross-sections* (with units cm²) for the various transitions of a given constituent, as a function of wavelength.

Atomic physics gives the cross-sections σ [cm²] and the physical conditions of the gas determine the population n_i [cm⁻³] of a given energy level. The mass absorption coefficient is then

$$\kappa_i = \frac{\sigma n_i}{r_i \rho_0}.$$

These coefficients are often given for $P = 1$ atm and $T = 273$ K, so that a correction is therefore required to take into account variations of altitude. At an altitude z_0 , the *optical depth* along a vertical line of a constituent i with mixing ratio $r_i(z)$ is given by the expression

$$\tau_i(\lambda, z_0) = \int_{z_0}^{\infty} r_i(z) \rho_0(z) \kappa_i(\lambda) dz,$$

where $\rho_0(z)$ is the mass density of the air.

The attenuation of an incident ray of intensity I_0 , received at altitude z_0 , and making an angle θ to the zenith (*zenith distance*), is

$$\frac{I(z_0)}{I_0(\infty)} = \exp \left[-\frac{1}{\cos \theta} \sum_i \tau_i(\lambda, z_0) \right],$$

where the sum is over all absorbing species.

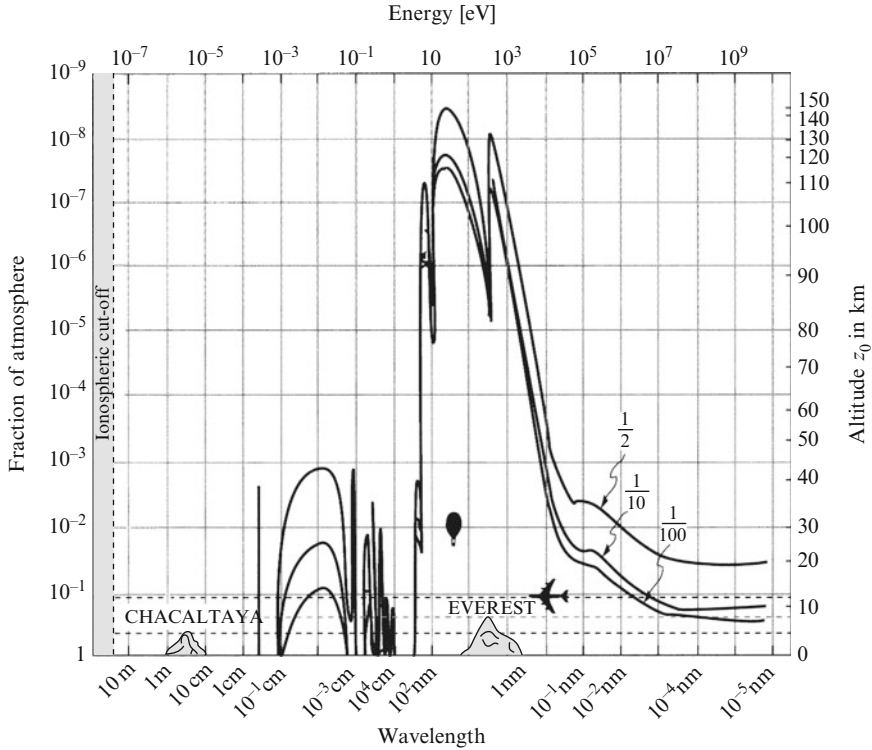


Fig. 2.4 Attenuation of electromagnetic radiation by the atmosphere. Curves give the altitude z_0 (right-hand scale) or the residual fraction of the atmosphere, in mass, above z_0 (left-hand scale), for three values of the ratio $I(z_0, \lambda, \theta = 0^\circ)/I_0(\infty, \lambda)$. Chacaltaya is a site in the Andes (altitude ~ 6000 m)

Figure 2.4 gives, as a function of wavelength, the altitudes z_0 at which the ratio $I(z_0, \lambda, \theta = 0^\circ)/I_0(\infty, \lambda)$ takes the values 0.5, 0.1, 0.01, respectively, which correspond to optical depths of 0.69 (transparent), 2.3, and 4.61 (opaque), again respectively. This figure covers the whole electromagnetic spectrum, from the cutoff at $\lambda = 23$ m (radiofrequencies), caused by the ionospheric plasma, right through to γ radiation at several GeV.

The atmosphere is totally opaque if $\tau_0 = 10$, and astronomical observation can be regarded as feasible when $\tau(\lambda, z) < 0.5$, implying transmission greater than 61%. Qualitatively, millimetre wavelengths are dominated by pure rotational bands of H_2O and O_2 ; the infrared and submillimetre region by rotational bands of H_2O and CO_2 , as well as by the rotational-vibrational bands of these constituents; and the near ultraviolet by electronic transitions of O_2 and O_3 . In the near ultraviolet, there appears the continuous absorption band of oxygen O_2 , which is characteristic

of the ionisation of this molecule in the ionosphere. The absorption continuum of N_2 dominates the far ultraviolet ($\lambda < 20$ nm).

At wavelengths less than 10 nm, molecular ionisation is complete and the absorption coefficient is effectively constant. The optical depth of a layer of thickness l [cm] is then given by

$$\tau_\lambda(\lambda \lesssim 10 \text{ nm}) \sim 30 l \text{ [cm]} \frac{P}{P_0} \frac{T_0}{T}.$$

For these wavelengths, even at the very low pressures encountered by stratospheric balloons ($z = 30$ km, $P = 10^{-3} P_0$), we obtain $\tau = 1$ (transmission 37%) for a very short path, of length $l = 30$ cm.

Figure 2.4 can be used to define the domains of ground-based and space-based astronomical observatories:

- *Ground-based astronomy* is limited to the visible, the near infrared ($\lambda < 25 \mu\text{m}$), where there remain, nevertheless, many absorption bands, millimetre wavelengths ($\lambda > 0.35$ mm), subject also to some absorption, and then centimetre wavelengths and beyond.
- *Space-based astronomy* covers all the rest of the electromagnetic spectrum, including γ -ray, X-ray, ultraviolet (UV) and infrared (IR). It should be noted, however, that the 50% transmission level occurs at quite different altitudes for different wavelengths. X-ray and γ -ray astronomy would just be possible at altitudes attainable by balloons (30 to 40 km), as would observation in the near UV ($\lambda > 200$ nm). Infrared and submillimetre observation is possible from an altitude of 12 km, which can be reached without difficulty by commercial aircraft (Airbus, B747), or on the polar ice caps of the Antarctic plateau.

The relatively low cost of these intermediate observational platforms (aircraft and balloons) led to their intensive use in the period 1960 to 1980, although this use gradually decreased between 1980 and 1990, with the development of powerful space observatories. A good example is NASA's Kuiper Airborne Observatory (KAO), which observes in the infrared and submillimetre ranges using a 0.9 m telescope carried aboard a large transport aircraft; and a 2.5 m replacement for this telescope (SOFIA) is being prepared for launch. Another example is provided by a very large stratospheric telescope (2 m), flown by the CNES in the 1990s on a balloon going above 30 km altitude (PRONAOS). In the future, such platforms will probably be reserved for very specific missions, since most observations are now made from genuine orbiting observatories, each one specialised in some wavelength range and having its orbit optimised accordingly.

The complete control of observing conditions now within our reach has totally freed astronomical observation of electromagnetic radiation from atmospheric absorption and opened up an energy range extending over sixteen powers of ten. This is a considerable improvement on the octave of traditional visible wavelengths (350–800 nm).

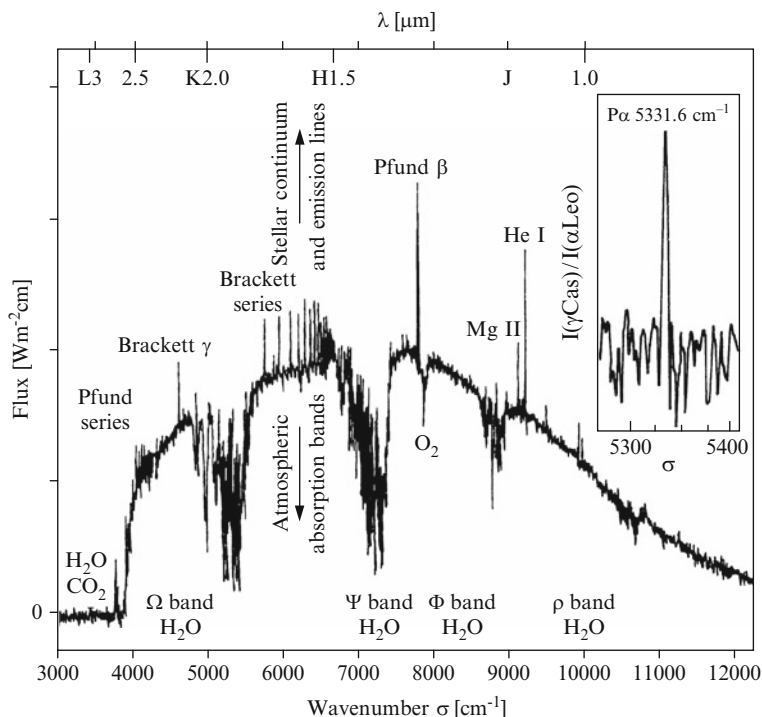


Fig. 2.5 Telluric absorption and spectroscopy: the spectrum of the star γ Cas. The spectrum was obtained using the 3.6 m Canada–France–Hawaii telescope at the summit of Mauna Kea, Hawaii, USA (4 200 m), with a Fourier transform interferometer (see Sect. 8.3.4), in the near infrared atmospheric transmission window, with a resolution of $\Delta\sigma = 0.5 \text{ cm}^{-1}$ (Chalabaev A., Maillard J.-P., *Ap. J.* **294**, 640, 1984). Atmospheric absorption bands are indicated, together with photometric windows I, J, and K (see Sect. 3.3). The star has both a continuum and emission lines (mainly H recombination lines). The *inset* shows the 3–4 Paschen α line (5331.6 cm^{-1}) extracted from a heavily absorbed part of the spectrum: the spectrum of γ Cas was divided by that of a reference star (α Leo) to eliminate atmospheric bands. As α Leo (spectral type B7) also has hydrogen lines, the absolute value of $P\alpha$ is not significant. Observation of $P\alpha$ would be impossible at lower altitude. (With the kind permission of the Astrophysical Journal)

Telluric Bands

In astronomical spectroscopy (see Chap. 8), the need often arises to distinguish a spectral line from a nearby atmospheric absorption band.³ Such a situation is illustrated in Fig. 2.5. A precise knowledge of the *profile* of the atmospheric absorption band is then required.⁴

³A detailed review of atmospheric bands in the radiofrequency range can be found in *Methods of Experimental Physics*, Vol. 12B. An inventory of telluric bands in the visible and near-infrared can be found in an atlas of the solar spectrum, where they arise as absorption bands.

⁴In millimetric astronomy, a very accurate measurement of the amount of water along the line of sight, combined with a careful model of the bands, can be used to almost completely eliminate them from observed spectra.

The profile of a molecular absorption band (rotational or vibrational–rotational) is generally a *Lorentz profile*, characterising lines in which the damping is dominated by collisions (pressure broadening). In the impact approximation (see AF, Sect. 2.20.2), the absorption cross-section thus has a frequency dependence $\phi(\nu, \nu_0)$, with the integral over all frequencies normalised to unity,

$$\phi(\nu, \nu_0) = \frac{\Delta\nu_L/2\pi}{(\nu - \nu_0)^2 + (\Delta\nu_L/2)^2},$$

where ν_0 is the central frequency of the transition, and $\Delta\nu_L$ is its total width. $\Delta\nu_L$ is related to the mean time τ between collisions according to

$$\Delta\nu_L = (\pi\tau)^{-1}.$$

This profile, illustrated in Fig. 2.6, gives a good representation of the cores of atmospheric bands, but generally underestimates the wings. The increase in the average attenuation with frequency is due to the cumulative effect of the wings of many weak H_2O bands. The attenuation is measured in dB km^{-1} and can be converted to optical depth by the formula $\tau = 0.23 \times \text{attenuation} [\text{dB km}^{-1}]$.

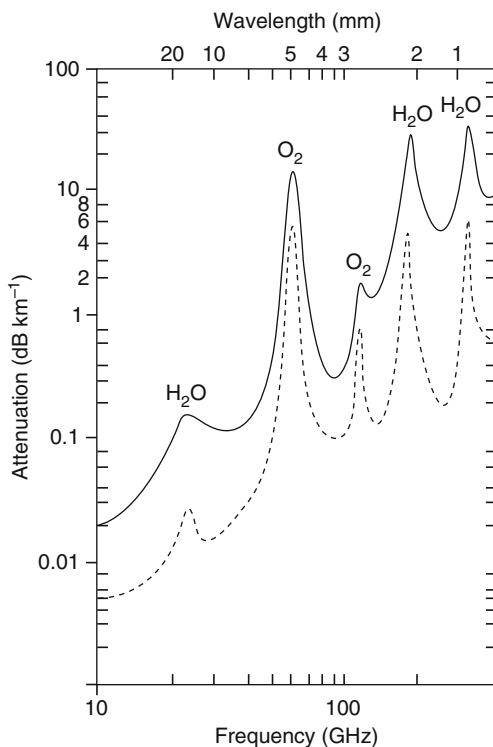


Fig. 2.6 Horizontal attenuation of radiation by atmospheric constituents, principally O_2 and H_2O , in the millimetre region. The constituents causing spectral bands are identified, and the band profiles are Lorentzian. Observation conditions: (continuous line) altitude 0.25 km, $T = 273 \text{ K}$, $\rho_{\text{H}_2\text{O}} = 7.5 \text{ g m}^{-3}$; (dashed line) altitude 4 km, $T = 273 \text{ K}$, $\rho_{\text{H}_2\text{O}} = 1 \text{ g m}^{-3}$

Ionospheric Plasma

The ionised, and hence conducting, layers of the upper atmosphere have a refractive index n related to the electron density N_e [cm^{-3}] by the expression

$$n^2 = 1 - \frac{\omega_p^2}{\omega^2} = 1 - \left(\frac{\lambda}{\lambda_p} \right)^2,$$

where the plasma frequency $\nu_p = 2\pi/\lambda_p$ is given by

$$\nu_p [\text{Hz}] = \frac{\omega_p}{2\pi} = \left(\frac{N_e e^2}{4\pi^2 \epsilon_0 m} \right)^{1/2} = 8.97 \times 10^3 N_e^{1/2}.$$

For example, the F -layer ($N_e = 2 \times 10^6 \text{ cm}^{-3}$) causes total reflection at $\lambda = 23.5 \text{ m}$ ($\nu \approx 12 \text{ MHz}$), the wavelength for which $n = 0$.

The ionosphere is thus generally transparent to both centimetre and millimetre wavelengths, a fact which explains the rapid development of ground-based radioastronomy.

2.3 Atmospheric Emission

The Earth's atmosphere emits photons, both by fluorescence and by thermal emission. The ability to discriminate between this emission and that of the astronomical sources under study determines one of the main limitations for ground-based observation in the visible, infrared, and millimetre regions. It is necessary to study, not only the intensity and wavelength dependence of these emissions, but also their possible fluctuation in space and time. Apart from these photons, which arise through conversion of incident solar light radiation, the atmosphere can also generate photons as a result of other incident particles, e.g., electrons. This case is discussed briefly in this section, and in more detail in the next on γ radiation.

2.3.1 Fluorescent Emission

The recombination of electrons with ions, which have been produced by daytime reactions of photochemical dissociation, leads to the emission of photons. This is called *fluorescent emission*, because the probabilities of de-excitation are small, and emission may occur up to several hours after excitation. Fluorescent emission comprises both a continuum and emission lines. It is also known as *airglow* (Fig. 2.7) and can only be detected at night, being swamped by scattering (see Sect. 2.4) during the day.

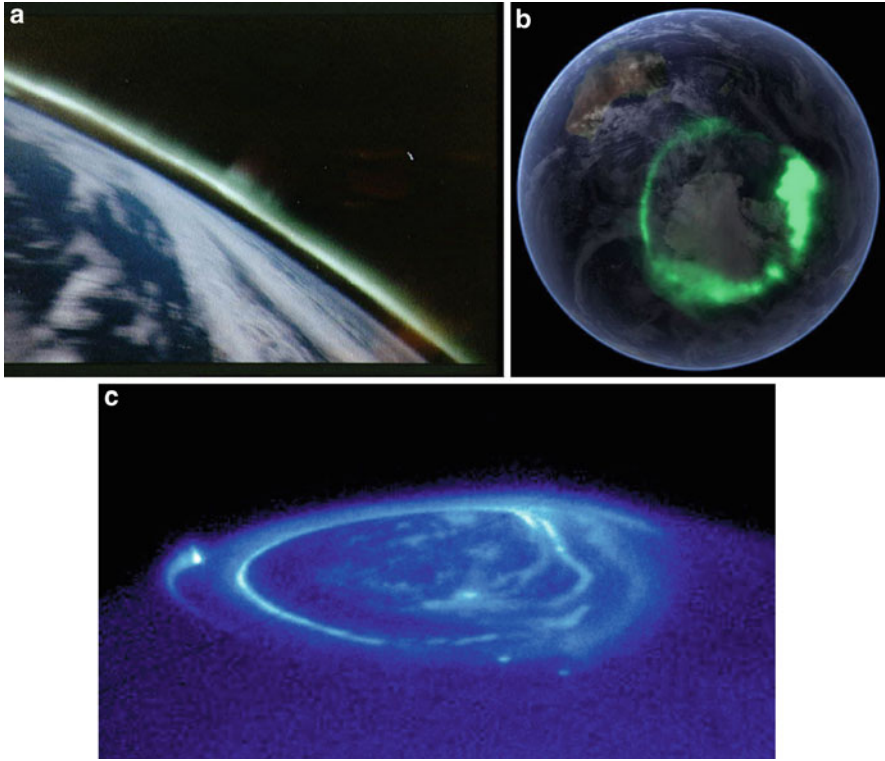


Fig. 2.7 (a) The Earth's atmosphere photographed tangentially from the Space Shuttle (mission STS-039, May 1991). One clearly sees the green airglow of the high atmospheric oxygen at altitude 80–120 km. The tangential observation increases the optical depth, hence the observed brightness (NASA). (b) The auroral ring above Australia, photographed by the NASA Image mission (2000–2006). (c) A polar aurora on the north pole of the planet Jupiter, photographed in the ultraviolet by the Hubble telescope (NASA/ESA, Clark J, University of Michigan). One sees the footprints of three of Jupiter's satellites (*from left to right*): Io, Ganymede, and Europa, creating currents in Jupiter's magnetosphere

Most fluorescence occurs at altitudes of around 100 km or above, where the density is low enough for spontaneous radiative decays, with spontaneous transition probability $A > 10^2 \text{ s}^{-1}$, to occur before collisional de-excitation.

The main sources of emission are the atoms and radicals O I, Na I, O₂, OH, and H. In the spectroscopic notation used by astronomers, O I is the neutral oxygen atom, O II is once-ionised oxygen, and so on. Emission intensity is measured in rayleighs [R], the unit being defined by

$$1 \text{ rayleigh} = \frac{10^6}{4\pi} \text{ photons cm}^{-2} \text{ s}^{-1} \text{ sr}^{-1} = \frac{1.58 \times 10^{-7}}{\lambda[\text{nm}]} \text{ W m}^{-2} \text{ sr}^{-1}.$$

Table 2.2 Atmospheric emission. R resonant scattering, C chemical reaction, I ionic reaction. Å denotes the old *angstrom* unit, $1 \text{ Å} = 0.1 \text{ nm}$. (After B.M. MacCormac, 1971)

λ [nm]	Emitter (state)	Altitude [km]	Intensity [rayleigh]	Process
102.5	H Ly β	200	10	R
121.6	H Ly α	10^2 – 10^5	2 000	R
260–380	O ₂ A ³ Σ_u^+	90	600	C
500–650	NO ₂	90	1 R Å^{-1}	C
557.7	O ¹ S	90–300	250	C, I
589.3	Na ² P	90	20–150	C
630	O ¹ D	300	10–500	I
761.9	O ₂	80	6 000	C

Table 2.2 summarises the main atmospheric fluorescences in the visible, and in the near infrared and ultraviolet. Note that, with the exception of auroral zones (magnetic latitude greater than 70°), in which ionisation is caused by injected electrons, the sky's emission varies little with latitude. Note also the presence of hydrogen emission lines caused by multiple resonant scattering of sunlight in the highest layers of the atmosphere (the hydrogen *geocorona*). The fluorescence of the radical OH is important in the near infrared (Fig. 2.8).

The Hubble Space Telescope, placed in low orbit, can easily measure the sky background. These measurements reveal (Caulet A. et al, *Astron. Astrophys. Suppl. Ser.* **108**, 1-8, 1994):

- Geocoronal emission at the wavelength of the Ly α (121.6 nm) line, with intensity from 3 to 20 k rayleigh, depending on the angle between the line of sight and the Sun.
- Emission by residual atomic oxygen OI, only measurable during the day, with intensity around 5 k rayleigh.
- A continuum of zodiacal scattering, in agreement with models of scattering by the zodiacal atmosphere (see Sect. 2.9.2).

Figure 2.9 gives the visible and ultraviolet magnitudes of the sky background, for observations from the ground and from space near the Earth. These magnitudes are given for a reference solid angle equal to one square arc second. They measure the flux produced by one square arc second of the sky background. Note the intensity of the geocoronal hydrogen Ly α (121.6 nm) line ($\sim 7 \times 10^{-3}$ photon $\text{s}^{-1} \text{ cm}^{-2} \text{ arcsec}^{-2}$). For wavelengths greater than 400 nm, the following correspondence is observed: a magnitude $m = 27 \text{ arcsec}^{-2}$ corresponds to a monochromatic flux of 10^{-7} photon $\text{s}^{-1} \text{ cm}^{-2} \text{ nm}^{-1} \text{ arcsec}^{-2}$.

The ready excitation of atmospheric components, so harmful to astronomical observation, is quite essential for the detailed study of the atmosphere in terms of local composition, temperature, and physical chemistry. The radar-like technique Lidar (LIght Detection And Ranging) involves excitation of atmospheric constituents, generally by tuneable laser, and the study of their de-excitation by measurement of re-emitted light. These techniques inspired a way of creating artificial stars, crucial for adaptive optics (see Sect. 6.3).

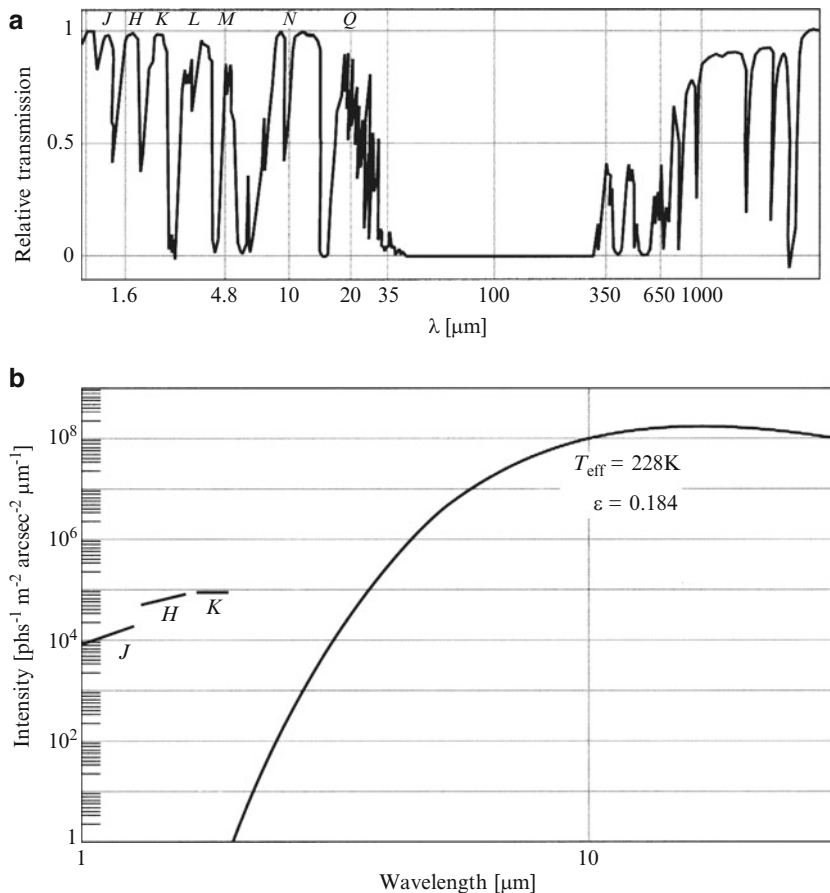


Fig. 2.8 (a) Atmospheric transmission (at altitude $z_0 = 4200\text{ m}$) across the whole infrared and submillimetre range. Spectral bands (see Sect. 3.3) are indicated with the usual notation. The relatively good submillimetre transparency corresponds to a quantity of precipitable water less than 1 mm. (b) Sky background brightness in the near infrared, at the altitude of Mauna Kea (4200 m). The blackbody temperature (indicated at the *top right*) which best represents the emission is $T = 228\text{ K}$, with an emissivity $\epsilon = 0.184$ [after Traub and Stier, 1976]. Upper limits for emission by the radical OH in spectral bands J, H, and K are indicated on the *left* (after McLean I., 1993)

Discrimination of Weak Astronomical Sources

The mean angular diameter of a stellar image, observed through the turbulent atmosphere of the Earth, is typically of the order of one second of arc (see Sect. 6.2.2), and consequently, it is usual to measure the sky background in magnitudes (the logarithmic units defined in Sect. 3.3) per square arc second.

We now calculate the magnitude of a square of sky background, with side one second of arc, which would correspond to fluorescence of intensity $1\text{ R}\ddot{\text{A}}^{-1}$ at 550 nm, using the fact that magnitude 0

corresponds to a monochromatic flux of $3.92 \times 10^{-8} \text{ W m}^{-2} \mu\text{m}^{-1}$:

$$\frac{1.58 \times 10^{-7}}{4\pi \times 550} \times (2.35 \times 10^{-11} \text{ sr}) \times 10^4 = 0.537 \times 10^{-17} \text{ W m}^{-2} \mu\text{m}^{-1} \text{ arcsec}^{-2}.$$

This gives $m_v(\text{sky}) = 24.6 \text{ arcsec}^{-2}$. Even using sky subtraction techniques between two neighbouring points, the space and/or time fluctuations of this emission would make it difficult to extract the signal of a galaxy with magnitude significantly less than $m_v(\text{sky})$ from a photographic plate or an electronically digitised image. A contrast less than 1% (that is, five magnitudes) is thus difficult to detect.

In addition, the development of imaging techniques at the diffraction limit of large telescopes (*adaptive optics*, see Sect. 6.3) requires great care to be taken over the grain of the background at high spatial frequencies. Without this attention, information at these frequencies could be lost.

The limit for observing very faint objects from the ground is thus set by the intrinsic emission of the night sky. There is a considerable gain in observing from space, as shown in Fig. 2.9, but there nevertheless remains a radiation background caused by the Solar System environment (see Sect. 2.9).

If the source has an intrinsic angular dimension much less than one second of arc, and if it is possible on the ground to reduce the effects of atmospheric turbulence, that is, reduce the solid angle of sky simultaneously observed, the sky background contribution will be greatly diminished. The contrast, and therefore the detection, will then be improved. This is the achievement of *adaptive optics* (see Sect. 6.3).

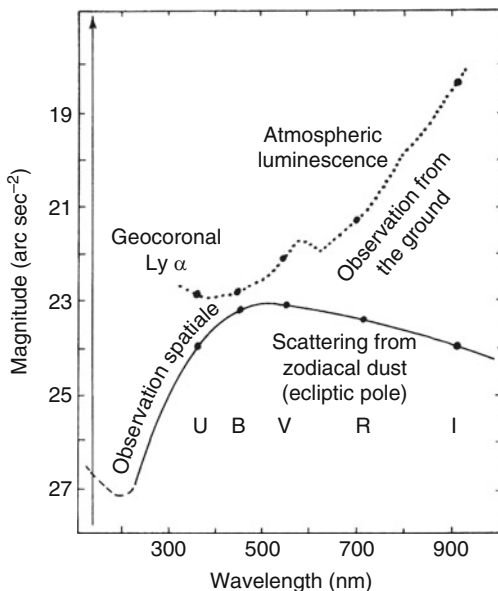


Fig. 2.9 Visible and ultraviolet magnitudes of the sky background per square arc second, for observations from the ground and from space near the Earth. Letters denote the spectral bands of the photometric system (see Sect. 3.3), corresponding to the points (●). (After Courtès G., personal communication; Smith H.E., Burbridge E.M., *Ap. J.* **210**, 629, 1979; Leinert C., *Sp. Sci. Rev.* **18**, 281, 1975; Machetto F. et al, *ESA-SP 1028*, 1980, European Space Agency)

2.3.2 Thermal Emission

The Earth's atmosphere can be considered as a gas in local thermodynamic equilibrium (LTE) up to an altitude of 40 to 60 km, beyond which collisions occur too infrequently to ensure the thermal population of all energy levels. A full radiative transfer calculation gives the specific intensity received at the ground for any given wavelength. A simple approximation is possible when the atmosphere is optically shallow, that is, when the optical depth τ_λ along the zenith line is much less than unity, corresponding to an atmosphere which is transparent at the wavelength considered. In this case the intensity received at altitude z and at zenith distance θ is

$$I_\lambda(z) = \tau_\lambda B_\lambda(\bar{T}) \frac{1}{\cos \theta},$$

where $B_\lambda(\bar{T})$ is the Planck function at the mean temperature \bar{T} of the atmosphere.

The wavelengths at which the two conditions $\tau_\lambda \ll 1$ and $B_\lambda(\bar{T})$ non-negligible are satisfied, correspond to the near infrared (1 to 20 μm) and millimetre (0.5–2 mm) atmospheric windows.

Table 2.3 gives the infrared magnitude (quantity defined in Sect. 3.3) of the sky per square arc second, in the zenith direction, taking $\bar{T} = 250 \text{ K}$ for the mean temperature in the emissive region of the atmosphere. These are, of course, mean values, and scatter about these values could be significant for some sites.

Detectable astronomical sources can be several orders of magnitude fainter than this sky emission. The problem of discriminating faint sources is similar to that encountered above for fluorescence.

The first part of Fig. 2.8 shows graphically the atmospheric transmission in the infrared and millimetre bands. The second part of the same figure shows a graph of atmospheric emission in the near infrared, from one of the best sites in the world for ground-based observation (the summit of Mauna Kea, Hawaii, $z_0 = 4\,200 \text{ m}$). On the first graph are shown the observational photometric windows defined in Sect. 3.3. On the second can be seen the extremely rapid growth of atmospheric emission on the Wien side of the Planck function $B_\lambda(T)$, leading to very high sky background emission at 10 μm (see also Table 2.3). At shorter wavelengths, thermal emission is overtaken by fluorescent emission of the radical OH. The spectral

Table 2.3 Mean thermal emission of the atmosphere. 1 jansky = $10^{-26} \text{ W m}^{-2} \text{ Hz}^{-1}$

Spectral band (see Sect. 3.3)	<i>L</i>	<i>M</i>	<i>N</i>	<i>Q</i>
Mean wavelength [μm]	3.4	5.0	10.2	21.0
Mean optical depth τ	0.15	0.3	0.08	0.3
Magnitude [arcsec^{-2}]	8.1	2.0	−2.1	−5.8
Monochromatic intensity [Jy arcsec^{-2}]	0.16	22.5	250	2 100

resolution of the second graph in the figure is not sufficient to resolve the discrete line structure of this emission, which severely limits detection sensitivity by ground-based observation between 1.6 and 2 μm .

It is in fact possible to design a comb-like spectral filtering device which, applied to the highly dispersed spectrum, cuts out these unwanted atmospheric bands and makes it possible to search for faint galaxies, for example. In the mid-1990s, this idea was applied to several telescopes, in particular the Japanese 8.2 m Subaru telescope in Hawaii, where it is now operational (see Sect. 5.2).

It is essential to make careful measurements of the precipitable water vapour when seeking new sites for infrared and millimetre observatories (see Sect. 2.8). To this end, a *spectral hygrometer* is used. This is a differential photometer, which compares the emission received at one wavelength (around 13 μm), where the atmosphere is entirely opaque and thus radiates practically like a black body ($\bar{T} = 250\text{ K}$), with the emission received at a wavelength (1.8 or 6 μm) dominated by an H_2O emission line, and whose optical depth is close to unity, in order to be as sensitive as possible to the value of $h_{\text{H}_2\text{O}}$. An example would be $\lambda = 6\text{ }\mu\text{m}$, for which the absorption coefficient is $\kappa(\text{H}_2\text{O}) = 10^2\text{ cm}^2\text{ g}^{-1}$, whence $\tau(\text{H}_2\text{O}) = 0.1$ when $h_{\text{H}_2\text{O}} = 0.1\text{ mm}$, a typical value for a site of exceptional quality such as the Antarctic plateau.

This thermal emission fluctuates in time because of the turbulent motions of the atmosphere. The temporal power spectrum for these fluctuations is generally inversely proportional to the frequency.⁵ The emission also fluctuates with the line of sight, as the flux integration is carried out over differing air masses. The result is a granularity of the thermal sky background emission which is a source of noise in some observations (see Sect. 9.4).

2.3.3 Differential Measurement Techniques

The intense emission of the atmosphere and the sensitivity of detectors make it essential to use *differential measurement* to eliminate sky background radiation, whether it be of thermal or fluorescent origin.

This applies to the detection of faint sources in the visible (magnitude $m_v > 15$), just as in the infrared, submillimetre, and millimetre ranges. It becomes imperative, even for a bright source, near $\lambda = 10\text{ }\mu\text{m}$, where the maximum for atmospheric thermal emission is located. Even for a small pixel, for example, several seconds of arc across, the intensity received from the atmosphere can be several times greater than that of the signal received from the source.

The same is true in the millimetre range, where the exceptional sensitivity of detectors allows detection of atmospheric emission quite far from its maximum. Consider, on Fig. 2.6, the wavelength $\lambda = 2.6\text{ mm}$ of a well-studied transition of the ^{12}CO molecule. The atmospheric transmission at a good quality site ($z_0 \sim 2\,000\text{ m}$),

⁵A quantitative analysis can be found in Käufl et al., *Exp. Astron.* **2**, 115, 1991.

is around 76% at this wavelength, that is, $\tau(2.6\text{ mm}) = 0.27$. The atmospheric transmission therefore corresponds to an antenna temperature (see Sect. 7.5) of $0.27 \times 273 = 75\text{ K}$, or to a spectral flux of 10 Jy ($1\text{ Jy} = 10^{-26}\text{ W m}^{-2}\text{ Hz}^{-1}$), whereas the astronomical source under study may be much less intense, by three or four orders of magnitude.

To distinguish the source from the sky background in each of these cases, an *offsetting* or *on-off technique* is used, which involves pointing the telescope successively at the source and then at a neighbouring part of the sky, supposed to be free of sources. A neighbourhood of several minutes of arc is adequate, and the hypothesis that atmospheric emission remains spatially uniform over such a region seems to be borne out. Taking the difference between the two measurements, the signal of the source alone can be reconstituted (*subtraction of sky background*). However, new techniques in spectroscopy, using fibre optics (see Sect. 8.3), detect light, very locally, over several hundred pixels spread across a field of several minutes of arc. Subtraction of the sky background can then reveal spatial fluctuation residues, representing an additional *spatial noise*. We shall discuss this in more detail in Chap. 9 (see Sect. 9.4), which deals with the precautions needed to carry out this type of observation.

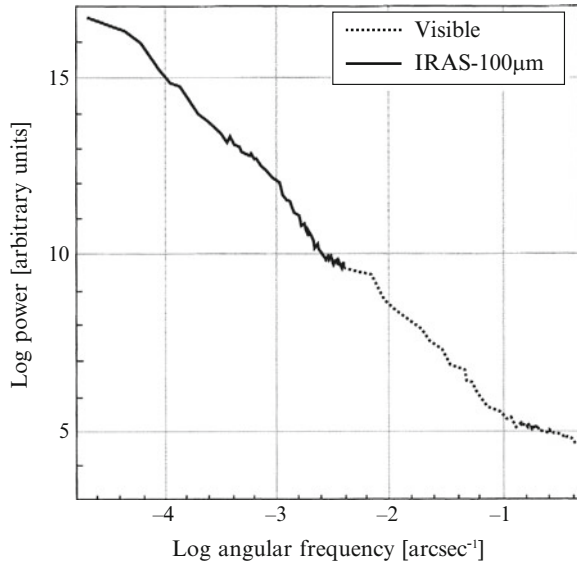
A second effect creates difficulties for this method. Atmospheric emission generally fluctuates in time (movement of invisible clouds of water vapour, variable excitation of fluorescence during the night, ionospheric winds, and so on), and the frequencies are rather high ($f \sim 0.1\text{--}10\text{ Hz}$). The differential measurement thus compares two emissions which differ randomly, and the result of the subtraction will be affected by a random noise, referred to as *sky noise*.

This noise is weaker as the modulation between the two fields increases. To use this fact, the secondary mirror of a Cassegrain or Coudé telescope (see Chap. 5) is given a sinusoidal, or better, a square-wave vibration which displaces the source image on the diaphragm determining the field (*sky chopping*). Meanwhile the thermal emission produced by the telescope itself, which also crosses the field diaphragm and reaches the detector, is kept absolutely constant. Radiotelescopes are generally too large, and so have too great an inertia, to allow this rapid modulation ($> 1\text{ Hz}$) of the pointing or of the secondary mirror. It is thus usual to obtain modulation by applying the on-off technique to the whole instrument, although naturally this is less fast.

To be more precise, the beam is displaced on the primary mirror during modulation by the secondary mirror, since the *field diaphragm* is generally chosen to be the secondary mirror itself. Any variation, even minimal, in the temperature or emissivity of the primary mirror then produces a further modulation, called the *offset signal*. These signals which cause very significant perturbation, are discussed in Chap. 9. It is this effect which renders infrared and millimetre measurements so difficult, and which disappears whenever it is possible, in space, to cool the telescope itself.

The principle of differential modulation has been described here in the context of dealing with atmospheric background emission, but it applies equally well in any situation where the problem is one of distinguishing a weak and spatially restricted source from a more or less uniform and bright background. Thus the detection of infrared galactic sources requires elimination of the zodiacal background (see Sect. 2.9.2). The same is true in the search for fluctuations in the diffuse cosmological background, which are of the order of 10^6 times less than the mean radiative background and require, this time in the submillimetre range, a subtraction of galactic interstellar emission. Figure 2.10 shows the grain of this galactic background quantitatively, by its spatial power spectrum.

Fig. 2.10 Power spectrum of sky brightness as observed from an orbit around the Earth, in the direction of the North Galactic Pole, at $\lambda = 100 \mu\text{m}$. *Continuous curve* : low frequency part sampled by the satellite IRAS (1983) with resolution 2 arcmin. *Dotted curve* : high frequency part deduced from CCD measurements in the visible. (After Low F.J., Cutri R.M., *Infrared Phys.* **35**, 29, 1994)



2.4 Scattering of Radiation

Atmospheric scattering is caused by the molecules which make up the air and by aerosols suspended in it. The vertical distribution of the former is directly related to density and thus decreases with altitude, whilst that of the latter is more capricious, depending on winds, climate, type of ground, volcanic activity, industrial pollution, and many other factors. The scattering of light by the brighter celestial bodies — the Sun and the Moon — gives rise in the daytime to the blue colour of the sky, and at night, to a veiling of faint astronomical sources. In the same way as atmospheric emission, scattering makes it difficult to discriminate faint sources. The highly chromatic nature of scattering only disturbs observation in the visible and very near infrared, for the day and night alike.

The molecular scattering in the visible and near infrared is *Rayleigh scattering*. The cross-section for Rayleigh scattering, integrated over all directions, is given by

$$\sigma_R(\lambda) = \frac{8\pi^3}{3} \frac{(n^2 - 1)^2}{N^2 \lambda^4},$$

where n is the refractive index and N the number of molecules per unit volume. The refractive index of air at $\lambda = 0.5 \mu\text{m}$ can be approximated by Gladstone's law, which gives

$$n - 1 \simeq 80 \times 10^{-6} \frac{P[\text{mb}]}{T[\text{K}]}.$$

Rayleigh scattering is not isotropic and $\sigma_R = \sigma_R(\theta, \lambda)$ is a function of the angle θ between the directions of the incident and scattered radiation [see *Astrophysical Quantities*, 3rd edn., Athlone, London 1973 (AQ), Chap. 5]. For an incident intensity I , the intensity j scattered into solid angle $d\omega$ is given by

$$j = \sigma_R \frac{3}{4} (1 + \cos^2 \theta) \frac{d\omega}{4\pi} I.$$

Even in the absence of any aerosols, the sky brightness due to Rayleigh scattering cannot be neglected. At an altitude of 2 000 m, at an angular distance $\theta = 90^\circ$ from the Sun, and at the wavelength of red light $\lambda = 700$ nm, the ratio of sky brightness to that of the Sun's disk is about 10^{-7} .

Aerosol scattering is governed by a different law, because the scattering particles are bigger than molecules.

The total effective cross-section of a sphere of radius a is given by Mie's theory as

$$\sigma = \pi a^2 (Q_{\text{scattering}} + Q_{\text{absorption}}).$$

The general theory of scattering by small particles can be found in the classic text by van de Hulst H.C., *Light Scattering by Small Particles* (Wiley, New York, 1957). Some useful results are also included in AF, Sect. 1.41.

If $a \gg \lambda$, $Q_s = Q_a = 1$, the scattered power is equal to the absorbed power, and the effective cross-section is twice the geometrical cross-section. If $a > \lambda$, Q_s and Q_a have a complicated λ -dependence, but for dielectric spheres (water droplets or dust grains such as silicates), the relation $Q_s \propto \lambda^{-1}$ holds, i.e., the scattered intensity varies as λ^{-1} .

The above description of the scattering of sunlight applies equally to the scattering of moonlight, whence infrared observation from Earth-based observatories is favoured on nights close to the full Moon. The scattering of urban lighting is also a problem (see Sect. 2.8).

Daylight Observations from the Ground

The thermal emission of the atmosphere grows exponentially (Wien part of the Planck curve) as the wavelength increases from the visible to the near infrared. Indeed, there is a wavelength beyond which this emission exceeds daytime scattering emissions, and hence in this range the brightness of the sky is largely independent of the day–night cycle. This is shown in Fig. 2.11. For telescopes with absolute pointing (i.e., to an accuracy of several seconds of arc, and without reference star), observations become feasible during the day. This could significantly increase the time available for use at large ground-based optical telescopes. Unfortunately, there are problems associated with the thermal control of instruments which limit this possibility. Of course, in the millimetre range, round-the-clock observation has become commonplace.

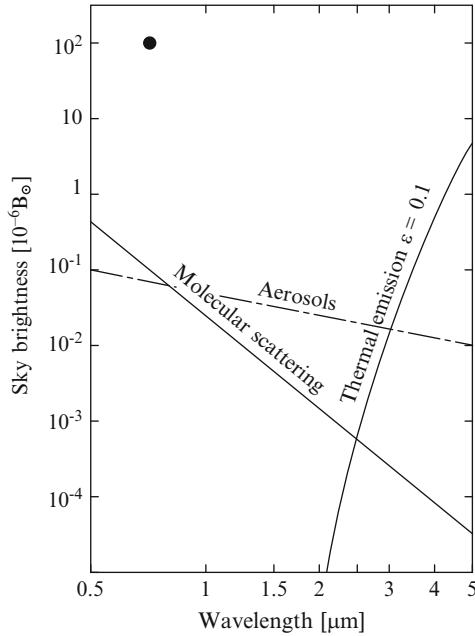


Fig. 2.11 Contributions to the sky brightness in the visible and near infrared. Molecular scattering is given for the altitude $z = 2000$ m, at 90° from the Sun. The wavelength dependence is λ^{-4} , and does not include correction for variation of refractive index $n(\lambda)$ with λ . Thermal emission is also shown, assuming uniform mean emissivity of 0.1, the exact value depending in particular on the quantity of precipitable water. The intersection of the two curves shows, in the absence of aerosols, the wavelength beyond which observation can be carried out during the night or the day regardless. The *dashed line* shows the possible additional contribution due to aerosols, varying as λ^{-1} , which moves the above wavelength threshold to the right. For comparison, (●) marks the sky brightness measured at 0.5 arcmin from the Sun's limb at an astronomical site (Kitt Peak National Observatory, Arizona. Source P. Léna, unpublished)

Solar Eclipses

Visible emissions from the solar corona immediately above the Sun's limb ($1.03 R_\odot$ from the centre of the disk, or 30 arcsec from the limb) are around 10^6 times less bright than the photospheric emission. The coronal emission is thus greater than the Rayleigh scattered intensity, but generally less than the light scattered by aerosols (*solar aureole*), which is generally quite considerable for scattering angles very close to zero (see Fig. 2.11).

Even from a high altitude site, observation of the white corona (continuous or *K* corona) is therefore very difficult, except during an eclipse of the Sun (see Fig. 2.12), for the intensity lies between 10^{-6} and 10^{-9} times that of the photosphere, and within just $1 R_\odot$ of the Sun's limb. On the other hand, for wavelengths at which chromospheric ($H\alpha$ line) or coronal (Fe XIV line at $\lambda = 530.3$ nm) emission is significant and quasi-monochromatic, atmospheric scattering can be practically eliminated by using a narrow filter. A ground-based coronagraph (see Sect. 6.6),

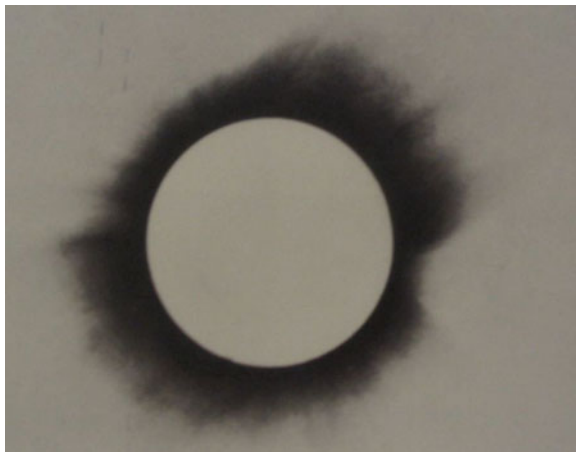


Fig. 2.12 The eclipse observation which confirmed general relativity. This photograph was obtained by the British astronomer Arthur Eddington during the total solar eclipse of 29 May 1919. By comparing the relative position of stars close to the solar limb with their positions on a photograph taken several months before, the deflection of light while grazing the Sun was measured and shown to be in agreement with the prediction made by Einstein on the basis of the curvature of space due to the Sun's gravitational field. Picture from the original article Dyson F.W., Eddington A.S., Davidson C., A determination of the deflection of light by the Sun's gravitational field, from observations made at the total eclipse of May 29, 1919, *Phil. Trans. R. Soc. Lond. A* **220**, 291–333, 1920

fitted with a filter, eliminates part of the instrumental and atmospheric scattering, which have values around 10^{-5} times the photospheric emission for a good site. This allows observation of the monochromatic corona out of eclipse. In space, only instrumental scattering remains and it is easier to observe the corona. Photospheric emission at X-ray wavelengths is negligible, and the X-ray corona can therefore be observed from space without the use of a coronagraph. Eclipses, although romantic events in the life of an astronomer, have had their importance diminished by space observation.

2.5 Atmospheric Refraction and Dispersion

The refractive index of air $n(\lambda)$ depends on the vacuum wavelength λ_0 . In dry air, between 0.2 and 4 μm , the following expression holds at pressure $P = 1$ atm and temperature $T = 15^\circ\text{C}$:

$$[n(\lambda) - 1] \times 10^6 = 64.328 + \frac{29498.1}{146 - 1/\lambda_0^2} + \frac{255.4}{41 - 1/\lambda_0^2},$$

where λ_0 is measured in μm .

At radiofrequencies (centimetre and beyond), refraction is hardly chromatic at all. Atmospheric refraction is manifested by a flattening of the solar disk at the horizon. Its dispersive character produces the *green flash* phenomenon at sunrise and sunset, and also the sometimes coloured appearance of stellar scintillation. More important for observation is the fact that the zenith distance θ' of a star is deviated from its true value θ . Refraction is a function of the thickness of air traversed, thus, for an atmosphere stratified in parallel planes, it is also a function of the quantity $m = 1/\cos\theta$, called the *air mass*. This effect is weak, but not negligible: $\theta' - \theta \sim -2''$ between 0.3 and 0.8 μm , for $\theta = 45^\circ$. In addition, there is chromatic dispersion, whence the coloured spreading in images of stars observed far from the zenith. These effects of differential refraction and dispersion cannot be ignored when angular resolution is significantly greater than 1 arcsec, which is the case in high resolution imaging, and more specifically in adaptive optics (see Sect. 6.3) and optical interferometry (see Sect. 6.4). A compensating optical device (an *atmospheric dispersion corrector*) must then be used.

The analogous effects of ionospheric refraction and dispersion are observed at radiofrequencies, since the refractive index of the ionospheric plasma is highly chromatic (see Sect. 2.2).

2.6 Turbulence Structure of the Earth Atmosphere

A static and homogeneous description of the atmosphere is clearly inadequate. It is a fundamentally variable medium, whose fluctuations have wide-ranging effects on astronomical observation, but cannot be described by a single model of those fluctuations. Its spatial fluctuations have wavelengths ranging from several thousand kilometres (depressions and anticyclones) down to millimetres (viscous dissipation); and likewise, its temporal fluctuations have time scales ranging from the secular, for certain climatic changes, to the millisecond, for image deformations.

In addition, these spatial and temporal variations are clearly not stationary. Large-scale spatial fluctuations ($\gg 1$ km) can lead to systematic effects, for example, errors in position determinations in *astrometry* resulting from corrections for atmospheric refraction (see Chap. 4). The present discussion will be limited to a description of effects on a small spatial scale ($\lesssim 1$ km), and a small time scale ($\lesssim 1$ s), these being typical scales at which atmospheric turbulence phenomena can directly affect astronomical observation.

The *stationarity* assumption, often inescapable in any reasonably simple statistical treatment, does not generally correspond to the reality in the context of observation. It is nevertheless possible, under this assumption, to derive a statistical description of atmospheric fluctuations, and to determine the various moments (mean, standard deviation) of those quantities which influence the propagation of electromagnetic waves. This will be dealt with in detail in Sect. 6.2, in the context of image formation.

2.6.1 Turbulence in the Lower and Middle Atmosphere

The layers under consideration here are the troposphere ($z \lesssim 12$ km) and possibly the lower regions of the stratosphere ($12 \lesssim z \lesssim 20$ km). We study here the way turbulence develops in these layers in the presence of winds, giving a rather simplified model, but one which satisfies our requirements.

A Simple Model of Turbulence

Turbulence develops in a fluid when the *Reynolds number*, a dimensionless quantity characterising the flow, exceeds a critical value. This number is defined as

$$\text{Re} = \frac{VL}{\nu},$$

where V is the flow velocity, ν the kinematic viscosity of the fluid, and L a characteristic length (e.g., diameter of the pipe in which the flow takes place, or width of an obstacle normal to the flow).

In air, $\nu = 1.5 \times 10^{-5} \text{ m}^2 \text{ s}^{-1}$. Taking $L = 15$ m and $V = 1 \text{ ms}^{-1}$, we obtain $\text{Re} = 10^6$, and this is far greater than the critical value $\text{Re} \approx 2000$ which corresponds to the transition from laminar to turbulent flow. For such high values of Re , turbulence is highly developed; the kinetic energy of large scale movements ($\sim L$) is gradually transferred to smaller scales of movement, with isotropisation, down to a scale l at which the energy is dissipated by viscous friction. The local velocity of a turbulent fluid is a random variable $V(\mathbf{r}, t)$ (see Appendix B), depending on the point \mathbf{r} and the time t . At any instant $t = t_0$, $V(\mathbf{r}, t_0)$ can be decomposed into spatial harmonics of the wave vector $\boldsymbol{\kappa}$, giving a further random variable $\vartheta(\boldsymbol{\kappa})$:

$$V(\mathbf{r}) = \iiint \vartheta(\boldsymbol{\kappa}) e^{2i\pi \boldsymbol{\kappa} \cdot \mathbf{r}} d\boldsymbol{\kappa}.$$

The mean kinetic energy (in the sense of an ensemble average) $dE(\boldsymbol{\kappa})$ in the interval between $\boldsymbol{\kappa}$ and $\boldsymbol{\kappa} + d\boldsymbol{\kappa}$, where $\boldsymbol{\kappa} = |\boldsymbol{\kappa}|$, is proportional to $\langle |\vartheta(\boldsymbol{\kappa})|^2 \rangle$, which is the power spectrum of the velocity $V(\mathbf{r})$. Straightforward dimensional analysis leads to the formula

$$V \propto (\varepsilon_0 R)^{1/3}$$

for the fluid velocity, where ε_0 is the rate of production (or dissipation) of turbulent energy, and R the scale under consideration ($R = 1/\boldsymbol{\kappa}$). We thus obtain

$$dE(\boldsymbol{\kappa}) \propto \boldsymbol{\kappa}^{-2/3} d\boldsymbol{\kappa}.$$

The dimensional argument mentioned above is based upon the following observation: at scales R which are large compared with the scale at which viscous dissipation takes place, the turbulent

velocity V should be independent of viscosity. Indeed, it should depend only on the energy production rate ε [$\text{J s}^{-1} \text{kg}^{-1}$], the scale R , and the mass density ρ of the fluid. The only combination of these quantities having the dimensions of a velocity is the one given above. See Landau L., Lifschitz E., *Fluid Mechanics* (Pergamon, Oxford).

By integration, we obtain the spectrum of the kinetic energy, known as the *one-dimensional Kolmogorov spectrum*,⁶

$$E(\kappa)d \propto \kappa^{-5/3},$$

provided κ is in the so-called inertial range

$$L_0^{-1} \lesssim \kappa \lesssim l_0^{-1},$$

where l_0 and L_0 are called the *internal* and the *external scale* of the turbulence, respectively. The assumed *ergodicity* (see Appendix B) of fully developed turbulence allows us to identify the ensemble and time averages

$$\langle |\vartheta(\kappa)|^2 \rangle = \langle |\vartheta(\kappa, t)|^2 \rangle_t.$$

Turbulence described by a $\kappa^{-5/3}$ one-dimensional power spectrum is said to be *homogeneous*. Outside the inertial range, the spectrum is governed by generation and dissipation processes. Near ground level, the value of the external scale L_0 varies between several metres and several hundred metres.

When turbulence occurs in a layer with a temperature gradient differing from the adiabatic one, it mixes air of different temperatures at the same altitude, and hence produces temperature fluctuations.

It can be shown that the equations governing velocity and temperature fluctuations are analogous, and that the one-dimensional spatial spectral density of the temperature fluctuations is

$$\Phi_\theta(\kappa) \propto \kappa^{-5/3},$$

where

$$\Phi_\theta(\kappa) = 4\pi\kappa^2 \left| \iiint \Theta(\mathbf{r}) e^{-2i\pi\mathbf{r}\cdot\boldsymbol{\kappa}} d\mathbf{r} \right|^2,$$

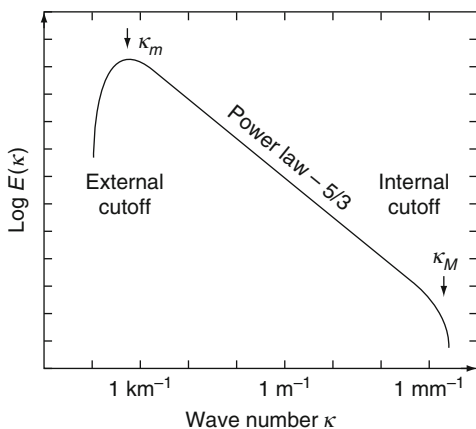
and $\Theta(\mathbf{r})$ is the temperature fluctuation about the mean $\langle T(\mathbf{r}) \rangle$

$$\Theta(\mathbf{r}) = T(\mathbf{r}) - \langle T(\mathbf{r}) \rangle.$$

More generally, Obukhov A.M. (Izv. Nauk. SSSR. Ser. Geograf. Geofiz. **13**, 58, 1949) has shown that the concentration of an impurity which is passive (i.e., does not affect the dynamics of

⁶Named after the hugely productive Soviet mathematician Andreï Kolmogorov (1903–1987). Apart from the first detailed study of turbulence, he also worked on signal processing, the subject of Chap. 9.

Fig. 2.13 One-dimensional power spectrum $E(\kappa)$ of the velocity fluctuations in a turbulent fluid, where the turbulence is isotropic and fully developed between the two scales L_0 and l_0 (turbulence obeying Kolmogorov's law in this interval). The corresponding wave numbers are $\kappa_m = 1/L_0$ and $\kappa_M = 1/l_0$. The ordinate is $\log E(\kappa)$. A variation in intensity of the turbulence (or of the energy injected at the scale L_0) results in a vertical shift of the curve



the fluid) and additive (i.e., does not react chemically) is also governed by the Kolmogorov law.

The spectral density of the temperature fluctuations also has low and high frequency cutoffs, just like the energy spectrum (Fig. 2.13).

It thus follows that the three-dimensional spectrum is

$$\Phi_T(\kappa) \propto \kappa^{-11/3}.$$

The covariance of the temperature fluctuations is defined by

$$B_T(\rho) = \langle \Theta(\mathbf{r})\Theta(\mathbf{r} + \rho) \rangle,$$

where $\langle \rangle$ denotes a mean over the space variable \mathbf{r} . $B_T(\rho)$ is the Fourier transform of $\Phi_T(\kappa)$ (Wiener's theorem, see Appendix B):

$$B_T(\rho) = \iiint \Phi_T(\kappa) e^{-2i\pi\kappa \cdot \rho} d\kappa.$$

This integral diverges if $\Phi_T(\kappa)$ follows the power law down to zero, but remains finite with the cutoff at $\kappa_m = 1/L_0$.

The *structure function* of the random variable $\Theta(\mathbf{r})$ is defined as

$$D_T(\rho) = \langle |\Theta(\mathbf{r} + \rho) - \Theta(\mathbf{r})|^2 \rangle,$$

and remains defined for all values of ρ , which indeed motivates the definition. It can then be shown, once again by dimensional considerations, that

$$D_T(\rho) = C_T^2 \rho^{2/3},$$

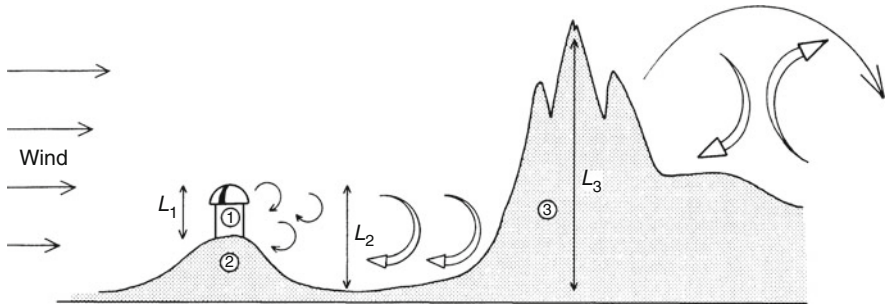


Fig. 2.14 Schematic representation of the generation of turbulence in the atmosphere by different obstacles. The amplitude of the temperature fluctuations depends on the amplitude of the turbulence and on the deviation of the actual temperature gradient from the adiabatic gradient. The scales L_1 , L_2 , L_3 are characteristic of the external scales of turbulence caused by wind around the obstacles 1, 2, and 3. Clearly, the choice of an astronomical observation site must take into account the prevailing winds and the relief upwind, as whirlwinds and eddies in turbulence damp down very slowly

and the three-dimensional temperature fluctuation spectrum is

$$\Phi_T(\kappa) = \frac{\Gamma(8/3) \sin(\pi/3)}{4\pi^2} C_T^2 \kappa^{-11/3} = 0.033 C_T^2 \kappa^{-11/3}.$$

C_T^2 is called the *structure constant* of the temperature fluctuations for homogeneous turbulence. The numerical value of C_T^2 characterises the intensity of the turbulence.

Turbulence in the atmosphere can be generated on different scales. Near ground level, the planetary boundary layer has thickness of the order one kilometre, and turbulence is produced by the flow of winds over surface (orographic) irregularities (see Fig. 2.14). Figure 2.15 shows a measurement of the vertical structure of turbulence in the first twenty kilometres above ground level. The structure constant $C_T^2(z)$ is determined locally by measuring the correlation in scintillation of the two components of a double star, using a technique called SCIDAR (SCIntillation Detection And Ranging).

The external scale L_0 is still not very well known. It varies enormously with the site and the conditions of excitation of the turbulence (wind), and its values range from several metres to several hundred, or thousand, metres. A good knowledge of L_0 is particularly important for optical interferometry (see Sect. 6.2.3), determining as it does the amplitude of the differential phase perturbation (*piston effect*) between two widely separated pupils.

At any altitude, the shearing motions of winds can produce a turbulent interface between layers in laminar flow. In the tropopause, this mechanism can lead to large values of C_T^2 , because of the high velocity (100–200 km h⁻¹) of the winds associated with the general circulation of the atmosphere (the jet stream). In addition, this general circulation can interact with large surface features (mountains) and cause gravity waves, which are likely to break in the non-linear regime of turbulent flow.

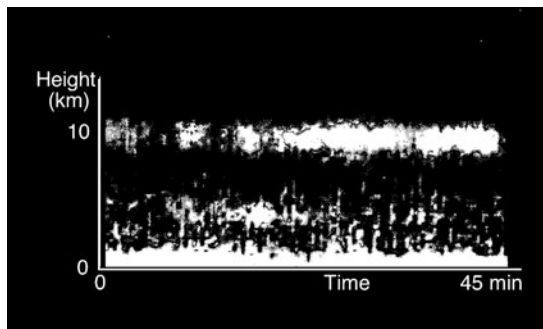


Fig. 2.15 Optical sounding of atmospheric turbulence. The *ordinate* gives the altitude and the *abscissa* the time (total duration of measurement was 45 min). The level of intensity gives the value of $C_T^2(z, t)$. The vertical resolution is ± 800 m, and the time resolution 20 s. Three turbulent layers can be seen: the *planetary boundary layer* near ground level, a layer at 4.8 km, and the layer at the tropopause (10–11 km). The sudden time variations show the intermittent nature of the turbulence. (Measurements carried out at the Observatoire de Haute-Provence, 1981, by Azouit M., Vernin J., J. Atm. Sci. **37**, 1550)

The criterion for the onset of turbulence caused by wind shear is given by the *Richardson number*

$$\text{Ri} = \frac{g}{T} \frac{\partial T / \partial z}{(\partial V / \partial z)^2},$$

where $V(z)$ is the wind velocity at altitude z . When $\text{Ri} < 0.25$, the flow generally becomes turbulent.⁷ This is a commonly occurring situation in the generation of terrestrial turbulence, when there is density and/or temperature stratification.

Strictly speaking, the quantity which should appear in the above expression is T_p , the *potential temperature*, and not T . The potential temperature is the temperature that a volume element of dry air would have if it were transformed adiabatically to a pressure of 1 bar.

It is thus possible, from a set of vertical soundings of the atmosphere (sounding balloons), to establish the distribution $C_T^2(z)$. The structure function $D_T(\rho)$ of temperature variations is measured at various altitudes using rapidly-responding thermal probes with spatial separation ρ . This distribution can also be measured from the ground using optical methods (Fig. 2.15), or indirectly from its effect on astronomical images, by determining the Fried parameter r_0 and its time development (see Sect. 6.2).

Knowledge of local turbulence is an essential parameter in the choice of an observing site.

⁷Woods J.D., Radio Sc. **4**, 1289, 1969, discusses the transition between laminar and turbulent regimes in atmospheric flow.

Temperature Fluctuations and the Refractive Index of Air

Fluctuations in temperature and the concentration of H_2O cause fluctuations in the refractive index of air. This can be written

$$n = n_0(T, C_{\text{H}_2\text{O}}) + ik(C_{\text{H}_2\text{O}}),$$

where the imaginary part k corresponds to absorption by H_2O and is important in the infrared and millimetre regions. (The concentrations of other constituents are ignored, their mixing ratios varying only by small amounts locally.) Fluctuations $\Delta n = n_0 - \langle n_0 \rangle$ of the real part can be written

$$\Delta n = \frac{\partial n_0}{\partial T} \Theta + \frac{\partial n_0}{\partial C} c.$$

For low values of the concentration $C_{\text{H}_2\text{O}}$, such as characterise astronomical sites, we obtain

$$\langle \Delta n^2 \rangle = \left(\frac{\partial n_0}{\partial T} \right)^2 \langle \Theta^2 \rangle.$$

As the fluctuations are isobaric, Gladstone's relation gives

$$\frac{\partial n_0}{\partial T} = \frac{80 \times 10^{-6}}{T^2} P,$$

for P in millibars (1 millibar [mb] = 100 pascal [Pa]) and T in kelvin [K]. The structure function for the refractive index can be written

$$D_n(\rho) = C_n^2 \rho^{2/3},$$

with a structure constant C_n related to C_T by

$$C_n = \frac{80 \times 10^{-6} P [\text{mb}]}{T^2 [\text{K}]} C_T.$$

Any fluctuation in the concentration of the absorber will lead to fluctuation in the imaginary part of the refractive index, and hence to fluctuation in the thermal absorption and emission of the volume element under consideration (*sky noise*, see Sects. 2.3.3 and 9.4).

As a first approximation, when studying the propagation of a wave, it is sufficient to know the integral of fluctuations along the line of sight. Hence the atmospheric turbulence of a given layer is characterised by the product $C_T^2 \Delta h$ for the temperature, or $C_n^2 \Delta h$ for the refractive index, where Δh is the thickness of that layer. Table 2.4 gives some typical values of the latter product, which is the only relevant parameter in image formation (see Sect. 6.2), for thin layers (several hundred metres) situated at various altitudes.

Table 2.4 Typical intensities of atmospheric turbulence

Altitude of layer [km]	3	6	10
$C_n^2 \Delta h$ [cm ^{1/3}]	4×10^{-13}	13×10^{-13}	7×10^{-13}

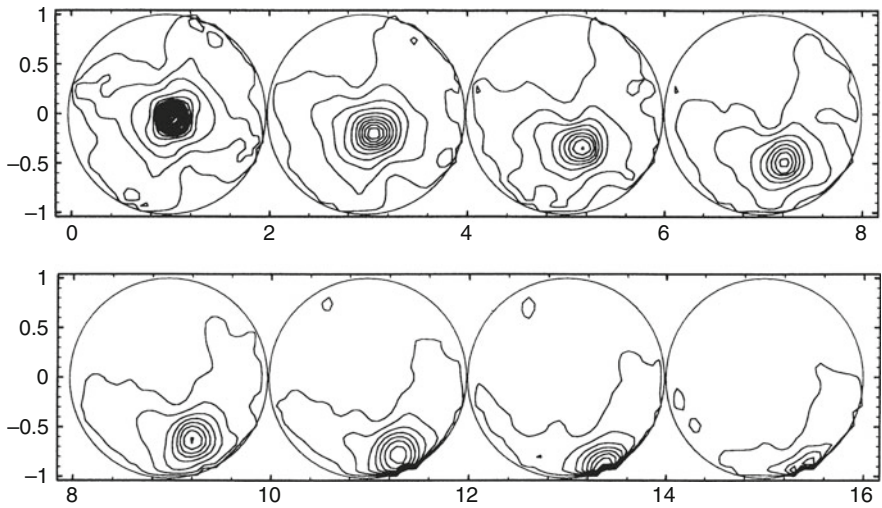


Fig. 2.16 Motion of a ‘frozen’ phase screen. The sequence of pictures shows the time development of the cross-correlation function (contours) of the phase of the wave emitted by a star (quasi-point source), reaching the circular pupil of a telescope (diameter $D = 3.6$ m) after crossing the atmosphere. The cross-correlation is calculated between time 0 and successive instants at intervals of 40 ms (see Appendix B). The uniform displacement of the cross-correlation peak can be clearly seen, pushed across by the wind, whose speed and direction can then be determined (14 m s^{-1}). 3.6 m ESO telescope, La Silla, Chile. (Gendron E., 1994)

Time Dependence of Turbulence

At a given point \mathbf{r} , the temperature is a random function $T(\mathbf{r}, t)$ of time. In the stationary case, it becomes possible to define a temporal power spectrum, characterising the time frequency content of the phenomenon (see Appendix B).

A simple model is made by considering the turbulence as ‘frozen’ (the *Taylor hypothesis*), with the above spatial power spectrum $E(\kappa)$, and assuming that a uniform wind is translating the air mass with velocity V (see Fig. 2.16). The temporal spectrum is then found by letting

$$\rho = V\kappa.$$

The temporal cutoff frequency is thus $f_c = V/l_0$, which gives, for $l_0 = 10 \text{ mm}$ and $V = 10 \text{ m s}^{-1}$, the value $f_c = 10^3 \text{ Hz}$. Indeed, this value is in good agreement with the order of magnitude of the highest frequencies observed in image deformation.

At a given site, the turbulence occurring in the various atmospheric layers, if indeed there are several, is generally a superposition of ‘frozen’ turbulence and of a turbulence which is more local, in the sense that it does not result from translation by a horizontal wind, but rather from vertical convection, for example near the tube or the dome of the telescope (*boiling*).

The physical origin of the Taylor hypothesis is simple: the time scales involved in development of turbulence are much longer than the time taken for a turbulent volume element, displaced by wind, to pass across the aperture of a telescope. It is therefore more correct to speak of a ‘frozen phase screen’, for a short time scale, than of ‘frozen turbulence’.

2.6.2 Ionospheric Turbulence

In the weakly ionised plasma which makes up the ionosphere, the electron density N_e fluctuates. The expression for the refractive index $n(\nu)$ is

$$n(\nu) = \left(1 - \frac{\nu_p^2}{\nu^2}\right)^{1/2}.$$

Observation reveals that the relative electron density fluctuations are small.⁸ It is found that

$$\langle \Delta N_e^2 \rangle^{1/2} \simeq 10^{-3} \langle N_e \rangle.$$

The correlation function for the refractive index is well represented by a Gaussian distribution

$$\frac{\langle n(\boldsymbol{\rho})n(\boldsymbol{r} + \boldsymbol{\rho}) \rangle}{\langle n(\boldsymbol{\rho})^2 \rangle} \approx \exp \left[-\frac{r^2}{2a^2(\nu)} \right],$$

where $a(\nu)$ is a typical correlation length. For $N_e = 10^5 \text{ cm}^{-3}$ ($\nu_p = 45 \text{ MHz}$), it is found that a takes values between 0.1 and 1 km. The power spectrum, which is the Fourier transform of the autocorrelation function, is then also Gaussian.

2.7 The Atmosphere as Radiation Converter

2.7.1 Ground-Based Gamma-Ray Astronomy

The detection of photons with energies of several hundred GeV takes us into the regime of very high energy γ ray astronomy. Here an atmospheric emission that is at

⁸The book *Methods of Experimental Physics*, Vol. 12A, contains a detailed discussion of fluctuations in the ionospheric refractive index by T. Hagfon.

first sight undesirable is used to detect the γ radiation from sources of astronomical interest. The atmosphere can be considered here as a huge, indirect detector (in fact, an electromagnetic calorimeter) of γ radiation. The following could thus have been discussed in Chap. 7.

When high-energy γ rays of astronomical origins enter the atmosphere, they produce e^+e^- which emit other high-energy photons as they slow down. These photons in turn produce other pairs and the process repeats itself. In the upper atmosphere, the particles involved in these cascade reactions are relativistic, and in fact move faster than the speed of light for this medium, whence they emit Cherenkov radiation (see Sect. 7.6). This very short emission of blue light, lasting only a few nanoseconds, can be detected. The signal is nevertheless very weak and must be focused by very big mirrors to be recorded by photomultiplier tubes placed in their focal plane. Observation conditions are the same as for observatories in the visible region, i.e., the sky must be very clear and without light pollution. The short duration of the Cherenkov signal is used to eliminate photon noise due to night sky emission, whence the main source of noise is in fact from cosmic radiation. Indeed, high-energy cosmic charged particles produce air showers, analogous to those initiated by γ -rays photons. Only a careful analysis of events can distinguish one effect from the other.

2.7.2 Air Showers and Cosmic Rays

When a proton or charged heavy nucleus of cosmic origin reaches the Earth, it will collide with a nucleus in the upper atmosphere, thereby producing a large number of secondary particles. The latter, which share the energy of the incident particle, will in turn collide with other atmospheric nuclei, creating an even greater number of high-energy particles. This process is repeated right down to ground level, where billions of particles of many different kinds are observed, covering an area of several tens of square kilometers. The first ground-based or balloon-borne cosmic ray observatories sought high altitudes in order to be closer to the primary source of the shower (the French cosmic ray laboratory which operated between 1940 and 1950 was situated at 3842 m on the Aiguille du Midi in the Mont Blanc massif, France). We shall examine the many uses of this phenomenon in Chap. 7.

2.8 Terrestrial Observing Sites

The high cost of a modern observatory makes it essential, for ground-based observation, to choose the best possible site, whatever logistic difficulties it may involve. It is quite probable that there are very few exceptional sites, taking into account the criteria mentioned in the following, which refer, firstly, to the

visible, infrared and millimetre ranges, and then to radio waves (centimetre and above).⁹

2.8.1 Visible, Infrared, and Millimetre Observations

The visible and infrared wavelength range is $\lambda \lesssim 30 \mu\text{m}$, while the millimetre wavelength range is $\lambda \gtrsim 0.5 \text{ mm}$. Criteria common to the choice of these sites are: absence of cloud, photometric quality, infrared and millimetre transparency, and image quality.

Cloud Cover

Tropical and desert regions are clearly the best with regard to satisfying this criterion. In such regions, diurnal convection, caused by large increases in surface temperature, can lead to cloud formation, especially around mountain peaks. The most favourable situation is one in which temperature inversion occurs (Fig. 2.17), stabilising those layers closest to ground level and preventing the cloud layer from rising above the inversion layer. Such a configuration exists at the volcanic peaks of Teide and La Palma (Canary Islands), and Mauna Kea (Hawaii), and also along the coastal mountain ranges of Chile and Namibia. Satellite surveys of the Earth provide information accurate to resolutions of around ten metres (Spot satellites).

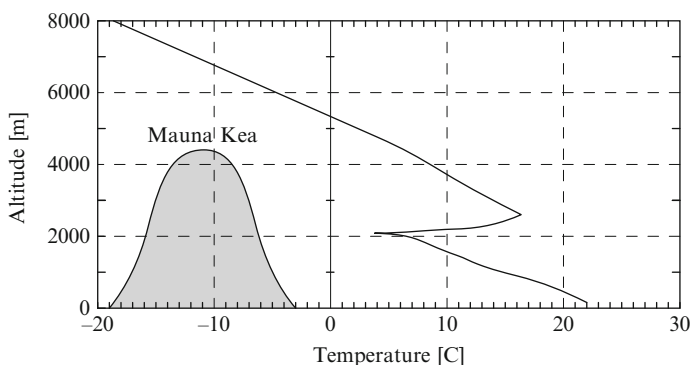


Fig. 2.17 Inversion layer above the Pacific Ocean, near the island of Hawaii (latitude 30° N). This is a *subsidence inversion*, caused by reheating of cold, descending air layers; the latter movement is itself caused by the general circulation of the atmosphere observed in *Hadley cells*. (Sounding balloon measurements, kindly communicated by P. Bely and the Hilo Weather Bureau, Hawaii, USA)

⁹An excellent review of the problems involved in selecting sites for optical astronomy can be found in *Site Testing for Future Large Telescopes*, European Southern Astronomy Workshop, J.P. Swings, Ed. Garching, 1983. See also the bibliography at the end of the book.

Regions with the least cloud are located in two bands on either side of the equator (10° to 35° N and 0–10° S to 35–40° S), but fluctuate over different longitudes.¹⁰

Photometric Quality

The photometric quality of a site refers to the stability of atmospheric transparency in the visible. The necessary photometric quality is considered to be reached in the visible when there are six consecutive hours of clear sky, for this allows sufficient time to apply extinction corrections (see Sect. 2.2).

Fluctuations in transmission are then of the order of 2%, or about 0.02 magnitudes. The above criterion is inadequate for infrared observation, affected by the passage of invisible clouds of water vapour, which mean that considerable fluctuations in IR transmission can coexist with an apparently clear sky.

Infrared and Millimetre Transparency

It was shown above that atmospheric absorption, thermal emission, and the spatial and temporal fluctuation (grain and sky noise, respectively) of the latter are all harmful phenomena caused by the presence of water vapour. For this reason, the choice of a site requires minimisation of the height of precipitable water, a criterion which once again favours polar sites and dry tropical sites, with seasonally anticyclonic weather conditions, and high altitude sites, given that the scale height of water is of the order of 2 to 3 km in the lower troposphere (Table 2.5). For example,

Table 2.5 Column of precipitable water at various sites. Values of *h* are mean values and may be subject to large seasonal variations. (After Chandrasekar T., Sahu K.C., Desai J.N., *Infrared Phys.* 23, 119, 1983)

Site	Country	Altitude [m]	Mean column of precipitable water [mm]
South Pole	Antarctic	3 000	<1.0 (summer)
Jungfrauoch	Switzerland	3 570	2.8
Kardung La	India	5 200	1.5
Kitt Peak	Arizona	2 130	7.1
La Silla	Chile	2 440	3.9
Mauna Kea	Hawaii	4 200	2.2
Mount Lemmon	Arizona	2 600	4.9
Mount Palomar	California	1 706	6.0
Cerro Paranal	Chile	2 660	2.3
Chajnantor	Chile	5 100	<0.5
Tenerife	Canaries	3 600	3.8
Zelenchuskaya	Caucasus	2 070	5.7

¹⁰See Miller D.B., *Global of Cloud Cover*, U.S. Dept. of Commerce, 1971.

the site Cerro Chajnantor, in the Andes at the frontier between Chile, Argentina, and Bolivia, was chosen at the end of the 1990s to set up the Atacama Large Millimeter Array (ALMA) (see Sect. 6.5.1).

Image Quality

Variations in temperature, and hence in the refractive index of the air, perturb the phase of electromagnetic wavefronts (see Sect. 6.2). This in turn affects the quality of images and measurements at visible and millimetre wavelengths.

To first order, these effects on astronomical images are characterised by several parameters:

- The integral of the turbulence along the line of sight

$$\int_{z_0}^{\infty} C_T^2(z) dz \simeq \sum_i C_{T_i}^2 \Delta h_i,$$

where the summation is over i distinct turbulent layers of thickness Δh_i .

- The evolution time of the turbulence, which is directly related to wind speed V_i in the various layers.
- The external scale L_i of the turbulence in each of the layers.

A more careful analysis of the effects of turbulence on images shows that the same turbulence but occurring at different altitudes will have different effects on an image.

In addition, turbulence is clearly not stationary over the periods of time considered (days, months, or even years), and so the histogram of its intensity over time must also be taken into consideration. Thus a site of average quality which benefits from periods of exceptional quality, such as the Pic du Midi in the French Pyrenees, may be preferred to a site with more uniform quality.

Local effects due to surface irregularities, as shown in Fig. 2.14, are often the dominant ones in the generation of turbulence, and so general rules cannot be given. Each potential astronomical site must undergo an in-depth study.

2.8.2 Centimetre and Metre Wave Radioastronomy

Radiofrequency interference is the main cause of perturbation in this range, and its avoidance has guided the choice of sites such as the Nançay centimetre telescope (France), the Very Large Array (VLA) in New Mexico (USA), and the Giant Meterwave Radio Telescope (GMRT) in Pune (India).

Other criteria enter into the choice of a good site: the latitude, with a view to covering as much as possible of the two celestial hemispheres; the horizontal surface area available for setting up interferometers (the Very Large Array occupies an area about 35 km in diameter); and the accessibility. This last criterion will no

doubt become less and less relevant, given the possibility of remote control of observatories and transmission of their observational data. Completely automated space observatories have clearly demonstrated the feasibility of this procedure, which will be a characteristic feature of observatories in the twenty-first century.

2.8.3 Very High Energy Gamma-Ray Astronomy

The detection of very weak blue Cherenkov radiation from the upper atmosphere imposes the same conditions as for observatories observing in the visible and near infrared: clear skies, almost total absence of precipitation, and absence of light pollution. To satisfy these conditions, combined with the need to view the galactic center which can only be seen from the Southern Hemisphere, the site for the four 12 metre mirrors of the High Energy Stereoscopic System (HESS) was chosen in Namibia at the beginning of the 2000s (see Sect. 7.6).

2.8.4 Very High Energy Cosmic Radiation

The optimal altitude for direct detection of the particles producing extensive air showers, themselves created by very high energy cosmic rays, lies between 1 000 and 1 500 m. Sites must be flat over several thousand square kilometers so that radio links between detectors are not blocked by orographic features. In addition, the detection of near ultraviolet radiation (≈ 300 nm) produced by fluorescence of atmospheric nitrogen, itself excited by passing particles, involves similar constraints to those affecting observatories in the visible region of the spectrum.

The international Pierre Auger observatory,¹¹ located in the flat deserts of the Pampa Amarilla in the west of Argentina, uses two detection techniques: observation of Cherenkov radiation produced locally in 1 600 water tanks, and observation of fluorescence from atmospheric nitrogen.

2.8.5 Man-Made Pollution and Interference

Human activity generates many difficulties for the running of a modern observatory, with its extremely sensitive detectors. To name but a few: light pollution in the visible, radiofrequency interference, heat sources such as nuclear power stations, which modify microclimates, vibrations, industrial aerosols, and the risks of an over-exploitation of space in the vicinity of the Earth.

¹¹The French physicist Pierre Auger (1889–1993) observed cosmic rays at the Jungfraujoch observatory (Switzerland).

Light pollution results mainly from scattering of light from street lighting, by atmospheric aerosols and molecules.

The following empirical expression can be used to estimate light pollution:

$$\log I = 3 - 2.5 \log R + \log P,$$

where P is the population of a town in units of 10^5 inhabitants, R is the distance in kilometres, and I is the ratio of artificial intensity to natural intensity (see Sect. 2.3.1) at a zenith distance of 45° . A town of 100 000 inhabitants at 40 km thereby increases the brightness of the night sky by 10%. For a source of luminosity L lumens at a distance R , the expression becomes

$$\log I = -4.7 - 2.5 \log R + \log L.$$

Aeroplanes also perturb photographic plates with their light signals, as do artificial satellites with scattering of sunlight. Such objects often turn up on astronomical images!

These preoccupations are clearly analysed in Cayrel R. et al. (eds.), *Guidelines for Minimizing Urban Sky Glow near Astronomical Observatories*, IAU, 1980; in *Rapport sur la protection des observatoires astronomiques et géophysiques*, Académie des Sciences, Paris, 1984; and also in publications of the *International Dark Sky Association*, NOAO, Tucson, Arizona.

Radiofrequency pollution comes from various sources: fixed or mobile emitters, radiotelephones, radars, high voltage transmission lines, industrial ovens, and many others. Specific spectral bands essential for radioastronomy are protected as part of the general problem of allocating frequencies, and the International Astronomical Union has established a threshold of $2 \times 10^{-6} \text{ W m}^{-2}$ as the maximum tolerable level.

The question of man-made *vibrations* has become relevant with the advent of optical interferometry and the detection of gravitational waves, which both require a high degree of stability for the instruments, of the order of 10 nm rms or better. Up until now, tests carried out in good sites have always shown that natural micro-seismicity dominates over distant perturbations. It will nevertheless be essential to regulate nearby sources, in particular road traffic.

The control of *aerosols* and, more generally, the rejection of industrial effluents into the atmosphere is a general preoccupation in environmental protection. However, industrial activity and, in particular, mining, which may develop near to astronomical sites, has to be watched with great care.

For a while it was feared that *commercial exploitation of space* might lead to a proliferation of low orbit light sources (advertising, lighting of ground areas by large scale solar mirrors), and also of radio-reflecting screens, and stations producing energy transported by microwave beams. All these possibilities would represent a threat to Earth-based astronomical observation, but regulation, monitored by the International Astronomical Union (UAI), has been introduced to control this.

2.8.6 The Antarctic

The ice cap covering the Antarctic continent offers possibilities for astronomy which have hardly been investigated yet. The plateau, at a mean altitude of

3 000 m and reaching a maximum height of 5 140 m, includes a wide range of different sites which are already equipped for intensive geophysical study under international collaboration (the South Pole, and nearby peaks on which bases have been established: Dome A, Dome C).

The temperature is very low on this plateau, the tropopause lying practically tangent to ground level. The atmosphere is extremely dry, with a quantity of precipitable water which can be less than 0.1 mm. Transmission in the infrared, submillimetre, and millimetre regions is certainly higher than anywhere else on the Earth's surface, and the emissivity correspondingly weak, both factors which contribute to increasing sensitivity of observation. It is likely that turbulence is much reduced by the absence of both low altitude convection and the high altitude jet stream, the atmosphere being stratified with a weak vertical temperature gradient. This fact also implies vastly improved image quality. Indeed, the systematic analyses¹² of image quality, now carried out both in summer and winter alike, have shown that there is a weakly turbulent layer confined to within roughly 30 m of the surface (Fig. 2.18).

Furthermore, astronomical objects are observable at zenith distances which remain constant over long periods of time. This is invaluable for making uninterrupted time sequences, when studying solar or stellar oscillations, determining stellar oscillation periods, or observing temporal micro-variations, with sensitivity greater than one thousandth of a magnitude.

Antarctic sites manifest some similarities with space or Moon-based sites, providing a transition from more conventional terrestrial sites. The establishment of permanent, high capacity astronomical observatories seems a likely possibility during the twenty-first century, bearing in mind that some instruments (e.g., a 1.7 m millimetre antenna) are already operating at the South Pole, set up by the United States in 1995, while many projects are under assessment for the French–Italian Concordia Station at Dome C, under the impetus of the International Polar Year (2007–2008).

2.9 Observation from Space

Space travel, from its beginnings in 1959, has revolutionised astronomical observation. The equipment put into orbit, usually unmanned, has shown a steady increase in both size and complexity, and its lifetime in orbit around the Sun, the Earth, or other planets has also increased, reaching more than a decade in the case of the Voyager probes and the satellite IUE (International Ultraviolet Explorer).

In the present book we have chosen to leave aside the possibilities of *in situ* observations and measurements in the Solar System, exemplified in the many exploratory missions to the planets and their satellites. These missions would require a whole book for themselves, as already stressed in Chap. 1. We shall thus restrict

¹²This is a fast-moving area, but the many investigations into the quality of Antarctic sites can be followed at <http://arena.unice.fr>.

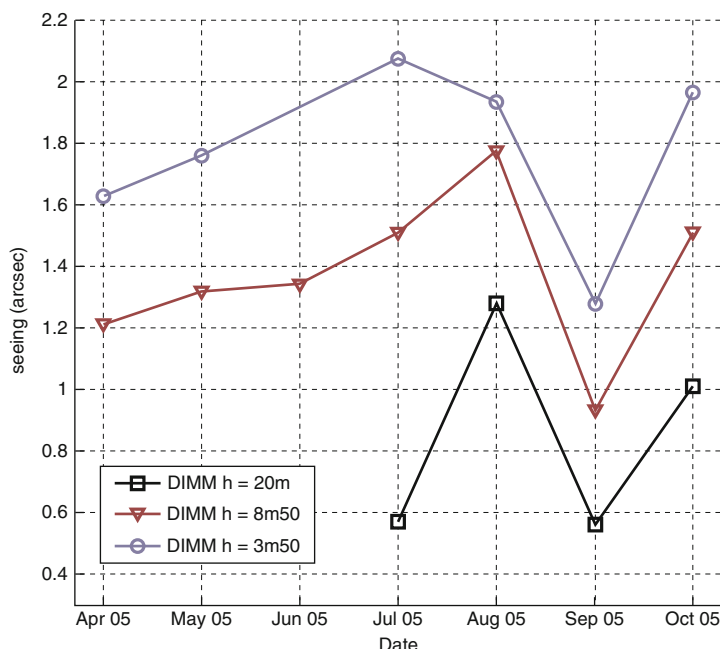


Fig. 2.18 Image quality at Dome C on the Antarctic plateau. The average size of a stellar image (seeing due to turbulence) is measured at different times of the year and at three different altitudes above the ground (3.5 m, 8.5 m, and 20 m), with an instrument called a *differential image motion monitor* (DIMM), used in site survey campaigns. These average values do not show the daily variability, which may occasionally reveal an exceptional seeing. From Aristidi, E., Fossat, E., Agabi, A., Mékarnia, D., Jeanneaux, F., Bondoux, E., Challita, Z., Ziad, A., Vernin, J., Trinquet, H., Dome C site testing, *Astron. Astrophys.* **499**, 955 (2009)

the discussion here to space observatories designed to observe the remote universe. A space observatory is not fundamentally different in principle from an observatory on the surface of the Earth. It contains telescopes, spectrographs, detectors, data processing equipment, and so on, the principles of which are dealt with in the following chapters. It is almost invariably unmanned, and therefore does not require any human intervention beyond remote control, although possibly in one of its more advanced forms, such as artificial intelligence or techniques involving virtual reality.

It is clearly not possible to cover all the details of space technology in this book. It is a fascinating subject, which includes many different aspects: the *launchers*, which determine the orbits and the mass of equipment; the *energy supply*, which determines manoeuvrability and data transmission capacity; the various *protection systems*, which fend off particles, micrometeorites, and the like, and the *cryogenic systems* which guarantee whatever lifetime is required for the mission; and the *quality control* and *reliability studies*, which test the system as a whole. Some of

these points are discussed briefly in the following chapters, in particular in Sect. 9.2, which deals with models for space observatories.

Traditionally, observations from atmospheric platforms, such as *aircraft* (10–20 km), *stratospheric balloons* (20–40 km), and *rockets* (up to 300 km), have been included under the denomination of space observation. Figure 2.4 shows the spectral ranges relevant to each of these platforms.

2.9.1 *The Advantages of Observation from Space*

The discussion earlier in this chapter has exposed three main causes of perturbation for astronomical observation: *absorption of radiation*, *turbulence*, and *interfering emissions*. The first of these considerably restricts access to the electromagnetic spectrum; the second affects image quality (resolution); and the third has a double effect, creating a uniform background from which faint sources must be extracted, but also, through *spatial fluctuations* (grain) and *temporal fluctuations* (sky noise), introducing a source of noise which reduces the sensitivity of observations.

Although atmospheric absorption practically disappears when an observatory is placed in low orbit ($z > 500$ km), some interference remains. Indeed, the transition is continuous between the upper atmosphere, the solar wind, with which it reacts (the magnetosphere), and the zodiacal dust cloud, which scatters the light from the Sun and emits its own thermal radiation. Moreover, the flux of particles coming from the Sun or diffusing through the Galaxy (cosmic rays) can interfere with detectors on board a space observatory, or even the materials they are made from. In the same way as the atmospheric signal, albeit invaluable for the study of the atmosphere, perturbs observation from the Earth, so the astronomical signals of nearby sources (the zodiacal nebula, the Sun, or even the Galaxy) are invaluable for the study of those sources, but perturb the observation of more distant and often fainter objects.

Some of these effects can be overcome by suitable choice of orbit; the problems caused by particles trapped in the terrestrial magnetosphere are to a large extent avoided by using low equatorial orbits (below 500 km) or very distant orbits (60 000 km and beyond). Other effects, such as zodiacal emission, are unavoidable as long as the orbit of the observatory is close to the Earth.

2.9.2 *Sources of Perturbation*

Although the conditions of observation from space are free from all those perturbing atmospheric phenomena which have been examined in this chapter, other perturbations come into play when an observatory has been put into space. These will be examined in the present section.

The Zodiacal Nebula

This is a distribution of dust grains in orbit around the Sun, in the neighbourhood of a plane of symmetry very close to the ecliptic (inclination $\sim 3^\circ$). The thermal emission from this zodiacal cloud is considerable, because of the temperature of the dust grains, heated by the Sun (~ 300 K at 1 AU). The spatial distribution of the dust grains, and also the distribution of their sizes, has been determined by studying the way they scatter sunlight (see Fig. 2.19).

The number of grains with radius between a and $a + da$, at a distance r from the Sun (measured in astronomical units), and at ecliptic latitude β , is given by

$$n(r, \beta, a) = N_0(a) \frac{a^{-k}}{r [\text{AU}]} \exp(-2.6 |\sin \beta|^{1.3}),$$

where the value of k determines one of the three grain populations involved, as shown in Table 2.6.

This early model [Frazier E.N., *Infrared Radiation of the Zodiacal Light*, SPIE **124**, 139, 1977] uses too high a value for the grain albedo (ratio of scattered to received energy), as shown by Mauser M.G., Ap. J. **278**, L19, 1984.

The monochromatic intensity received at the Earth can be expressed as

$$I(\lambda, \varepsilon, \beta) = I_S(\lambda, \varepsilon, \beta) + I_E(\lambda, \varepsilon, \beta),$$

where ε and β are the ecliptic coordinates of the line of sight (solar elongation ε and latitude β), and I_S , I_E are the contributions from scattered sunlight and intrinsic thermal emission, respectively.

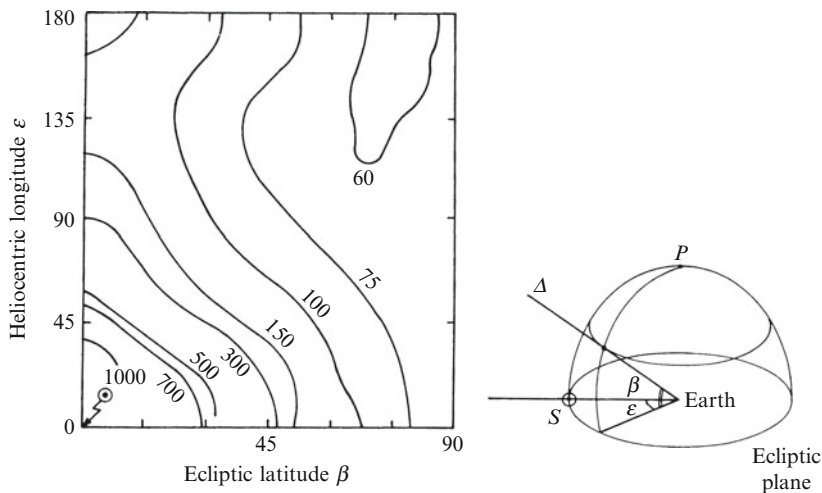


Fig. 2.19 Scattered zodiacal light. Isophotes of the scattered intensity measured in the direction Δ , characterised by its azimuth ε (measured from the Sun), and its ecliptic latitude β . P is the ecliptic north pole. The intensity contours are specified in S_{10} units, that is, in numbers of stars of magnitude $m_v = 10$ per square degree (see AQ, Sect. 73). For $S_{10} = 1$, the brightness at $\lambda = 540$ nm is $1.26 \times 10^{-8} \text{ W m}^{-2} \mu\text{m}^{-1} \text{ sr}^{-1}$, or $4.3 \times 10^{-16} \bar{B}_\odot$, where \bar{B}_\odot is the average brightness of the Sun at that wavelength. (Levasseur-Regourd A.C., Dumont R., Astr. Ap. **84**, 277, 1980)

Table 2.6 Size of interplanetary dust grains

a [μm]	k	N_0 [cm^{-3}]
0.008–0.16	2.7	10^{-12}
0.16–0.29	2.0	1.1×10^{-14}
0.29–340	4.33	1.9×10^{-17}

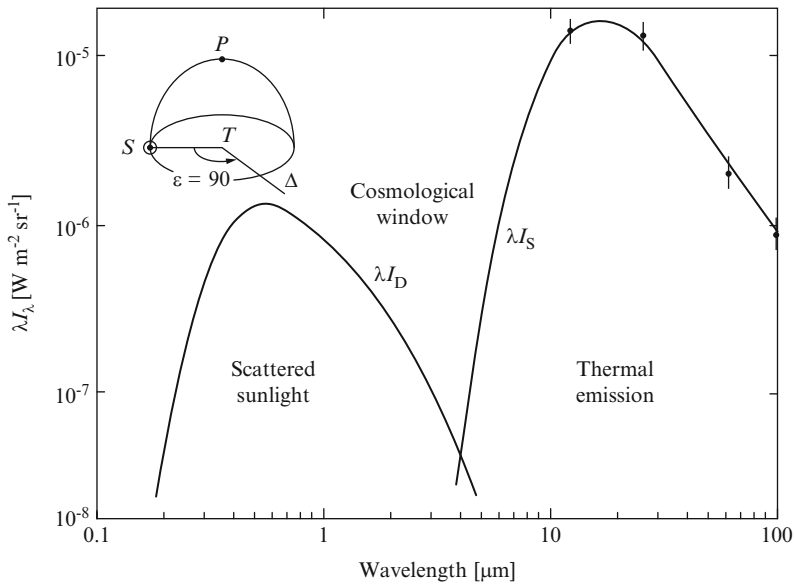


Fig. 2.20 Spectrum of zodiacal light in the visible and the whole of the infrared. The *ordinate* is the reduced brightness $\lambda I(\lambda)$. (The advantage of using this quantity is explained in Sect. 3.1.) The *inset* shows the line of sight Δ . The measurement points for I_S are from the satellite IRAS. (After Hauser M.G. et al., *Ap. J.* **278**, L19, 1984)

The scattered intensity I_S manifests exactly the colour of the Sun’s photosphere, which has colour index $(B - V)_\odot = 0.65$, to be compared with $(B - V)_S = 0.64$. The spatial dependence of I_S is shown in Fig. 2.19 (see also AQ, Sect. 84) and the spectrum is given in Fig. 2.20.

Figure 2.20 gives the radiated intensity of the zodiacal nebula in the whole of the infrared region. This intensity depends very much on the position of observation, which corresponds, in the figure, to a choice of orbit close to the Earth and a line of sight lying in the ecliptic plane, at 90° to the direction of the Sun. The emission is fitted to measurement points obtained by the satellite IRAS (InfraRed Astronomical Satellite, 1983). It can be well represented by the curve corresponding to grey grains of constant emissivity 3.8×10^{-7} , with a mean temperature of $T = 235$ K; but even better by the curve for grains of λ -dependent emissivity (in fact, a function of λ^{-1} , see Sect. 2.4), with temperature 164 K. Note the deep minimum between the scattered and thermal components, near $3.5 \mu\text{m}$. This minimum in the background emission due to the interplanetary ‘atmosphere’, is sometimes called the

cosmological window, permitting, as it does, observation of distant, and therefore faint, objects. At wavelengths above $100\text{ }\mu\text{m}$, great care must be taken to extract the contribution of the zodiacal nebula when measuring the weak signals of the cosmological background: the WMAP and Planck missions (the latter was launched in 2008) will thus refine our knowledge of this emission (see Sect. 7.4).

The observations made possible by this window may be carried out from the ground or from higher altitudes. The background zodiacal emission, which decreases as the wavelength increases from 1 to $3\text{ }\mu\text{m}$, makes way for atmospheric emission, or indeed emission from the instrument itself, should the latter not have been cooled. Hence, the point of minimum emission is shifted anywhere between $\lambda = 1.6\text{ }\mu\text{m}$ (for the non-cooled Hubble telescope, emissivity 0.2) and $\lambda = 2\text{ }\mu\text{m}$ (for a ground-based telescope optimised in the infrared, emissivity 0.03), but attaining its lowest value at $2.5\text{ }\mu\text{m}$ (as envisaged for a 6 m telescope project, at temperature 200 K, emissivity 0.03, to be carried by stratospheric dirigible at altitude 12 km over the Antarctic).

High-Energy Particles and Photons

Diffuse Cosmic Background

In the X and γ ray regions, this background (see Fig. 2.21) consists mainly of a superposition of emissions with different redshifts, originating in active galactic

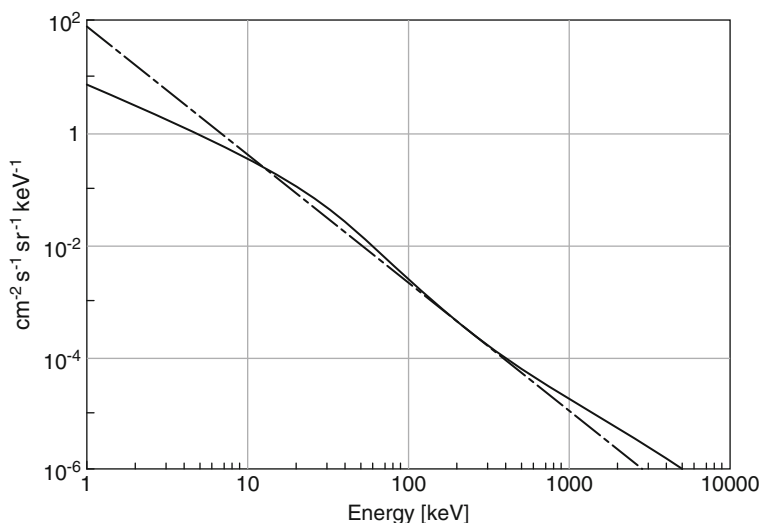


Fig. 2.21 Observed spectrum of diffuse electromagnetic cosmic background between 3 keV and 10 MeV (X and γ rays). The *straight line* represents the power law $E^{-2.3}$, which gives a good fit to the observations. (After Gruber D.E. et al., Ap. J. **520**, 124 1999)

nuclei (*quasars*, *Seyfert galaxies*). Visibility of a specific object in the field of view is reduced, because fluctuations in this cosmic background act as a source of noise when measuring the flux from the object. Between 10 keV and 1 MeV, the spectrum is governed approximately by the power law $I = 87.4 \times 10^{-2.3} \text{ cm}^{-2} \text{ s}^{-1} \text{ sr}^{-1} \text{ keV}^{-1}$. This source of noise, which dominates in the X region ($E < 50 \text{ keV}$), becomes negligible at higher energies ($E > 500 \text{ keV}$), where another background signal takes over, namely the one produced by interactions of charged particles with the detector and its environment. Collimators restricting the instrument's field of view are used to minimise background noise from this source.

Solar Wind

The solar wind is hydrogen plasma ejected from the Sun, which travels at high speeds along the field lines of the *heliosphere*. It varies with solar activity and its intensity determines the size of the heliosphere. In active solar periods, *solar flares* send huge quantities of particles into interplanetary space (see Fig. 6.37). The flux of particles can then increase by a factor of 1 000 for almost one day. Such events greatly perturb the running of observatories in orbit. Indeed, their measurements often become unusable, and the instruments, or even the spacecraft, may suffer considerable damage (e.g., electronic failure). It is of the utmost importance to assess the radiation impinging on each part of an experiment, and this throughout the mission, in order to select components of the appropriate quality (particularly, resistance to irradiation).

Radiation Belts

The trajectories of charged particles in the solar wind, electrons and protons, are modified by the lines of force of the Earth's magnetic field, and some particles are trapped in what are referred to as radiation belts (*van Allen belts*).¹³ The proton belt extends roughly between altitudes 1 000 and 15 000 km. The electron belts extend as far as 50 000 km, and at high geomagnetic latitudes have 'horns' which descend to low altitude. There are two belts, or two maxima, in the distribution of electrons, the main one being at about 20 000 km, with a secondary maximum at about 3 000 km (Fig. 2.22). Moreover, the motion of the geomagnetic axis relative to the axis of the Earth's rotation tends to bring the belts closer together in the austral region of the Atlantic ocean, and this creates the so-called *South Atlantic Anomaly* (Fig. 2.23).

¹³Named after US physicist and astronomer James van Allen (1914–2006), who discovered the radiation (in fact, particle) belts which carry his name during the first space flights (the Explorer mission in 1958).

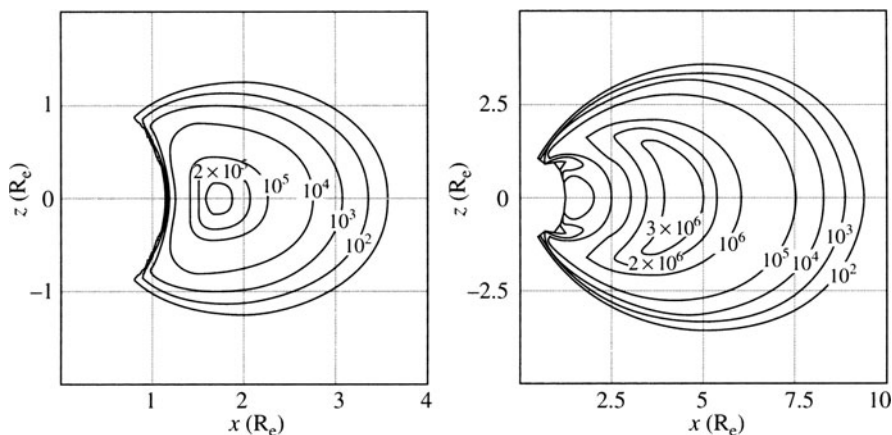


Fig. 2.22 Radiation belts of the Earth. Iso-intensity curves represent the mean flux, integrated over all directions, of electrons (*right*) and protons (*left*); z is the axis of the Earth's magnetic poles and x lies in the plane perpendicular to it, with units equal to R_e , the Earth's radius. Flux units are the number of particles $\text{cm}^{-3} \text{s}^{-1}$ above an energy threshold indicated in MeV. [After Daly E.J., Evaluation of the space radiation environment for ESA projects, ESA Journal **88** (12), 229, 1988]

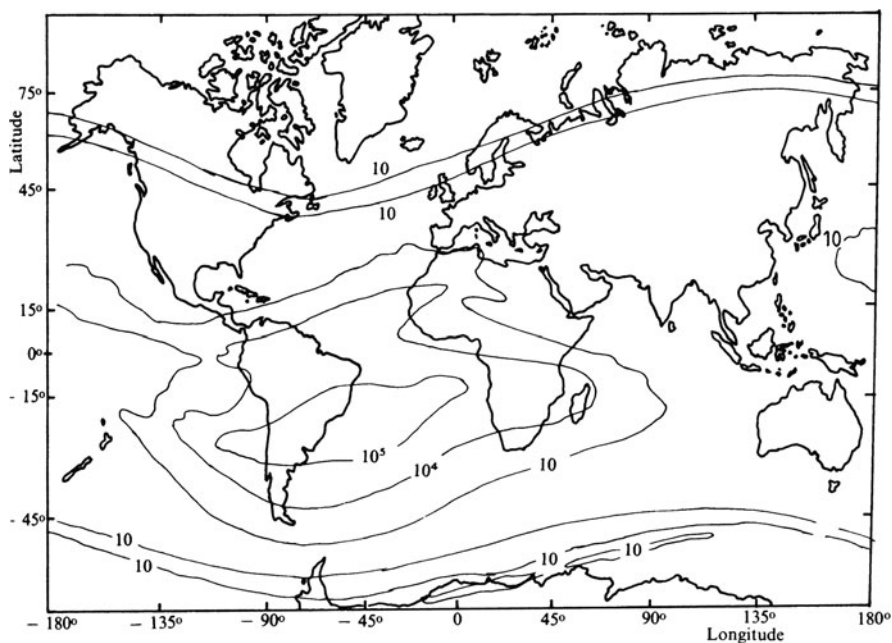


Fig. 2.23 Distribution of electron flux ($E > 5 \text{ MeV}$) at altitude 1000 km. Contours refer to number of electrons $\text{cm}^{-2} \text{s}^{-1}$. The flux is essentially directed along the lines of force of the Earth's magnetic field. Note the *South Atlantic Anomaly*, and the concentrations in the auroral zones. The data shown is only quantitatively correct for the epoch 1968–1970. (After Stassinopoulos E.G., NASA SP-3054, 1970. With the kind permission of E.G. Stassinopoulos)

Cosmic Rays

The protons, electrons, and nuclei comprising cosmic rays enter the Solar System and interact with the heliosphere, which opposes their penetration. The extent of the heliosphere, made by the solar wind, increases as the Sun is active, and hence the penetration of cosmic rays is governed by solar activity; the flux of cosmic rays in the neighbourhood of the Earth is maximum when solar activity is minimum, and conversely (Fig. 2.24). This phenomenon is called *solar modulation*. The Earth's magnetosphere also opposes the penetration of cosmic rays.

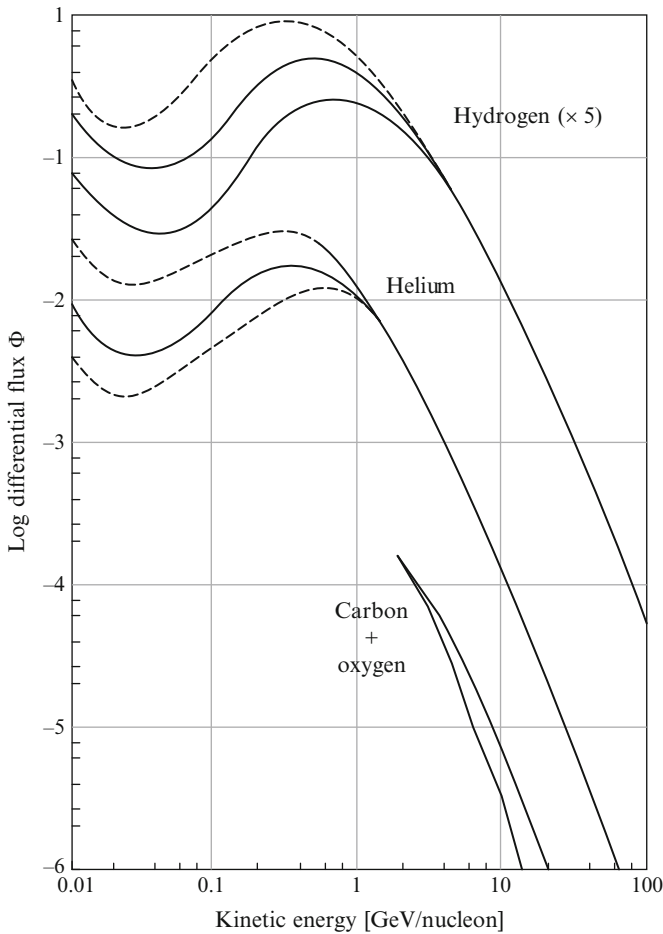


Fig. 2.24 Flux of cosmic ray particles outside the Earth's cavity, for various nucleons. The ordinate Φ is a differential energy distribution (number of nucleons considered $\text{m}^{-2} \text{sr}^{-1} \text{s}^{-1} \text{MeV}^{-1}$), and the abscissa is the nucleon energy. Modulation due to solar activity is visible at low energies: dashed curves indicate maximum and minimum levels of the solar cycle (upper and lower curves, respectively); continuous curves refer to mean solar activity. (After Webber W.R., Lezniak J.A., *Astrophys. Sp. Sci.* **30**, 361, 1974)

Background from Interaction with Surrounding Matter

Orbiting observatories, and all measurements they carry out, are affected by the arrival of these particles. Protons from the Sun or in cosmic rays induce *spallation* in all matter constituting or surrounding experiments. This matter thus becomes radioactive, emitting neutrons or γ rays, either immediately (instantaneous de-excitation), or after a lapse of time determined by the lifetime of whatever radioactive isotopes have been created. Hence, not only do charged particles interfere directly with γ -ray detectors, simulating the detection of high energy photons, but also the detectors are blinded by γ ray emission from de-excitation of surrounding matter.

This emission has a highly complex spectrum, containing many de-excitation lines superposed upon a continuous emission. This emission contributes to the background and limits the sensitivity of the experiment. As its spectrum has a slope less than the spectrum of diffuse emission, the former greatly exceeds the latter in the γ ray region. The contribution varies with the particle environment of the satellite, which is due to belts and cosmic rays, and therefore depends on the orbit, the position of the satellite on this orbit, and solar activity.

2.9.3 Choice of Orbits

With the advent of space travel, it has become possible to launch *probes* to make measurements, and to explore *in situ*, or in the vicinity of, objects in the Solar System; and also to launch *observatories* to measure electromagnetic radiation, for the main part, but possibly gravitational radiation in the future, which has been emitted from distant objects outside the Solar System, thus complementing in this case the role of ground-based observatories.

The choice of orbit for a probe depends at the outset on the object under study, e.g., the Moon, Mars, Saturn, cometary nucleus, and so on, the problem being one of organising an encounter, with the help of calculations in the realm of celestial mechanics. The aims of the observation dictate the choice of location for the observatory. But other factors must nevertheless be taken into account: the power and availability of launchers; the cost of the mission; and the location of receiving stations on the Earth or of relay satellites in direct view of the space observatory, given that rates of data production are often such that it cannot be stored even temporarily aboard, but must be continuously transmitted. A compromise is often necessary between the ideal location and the one eventually opted for.

In *low equatorial orbits* (300 to 500 km), which are used by the space shuttle and the International Space Station (ISS), communication is easy and repairs are possible. On the other hand, their lifetime is reduced by residual atmospheric friction, the Earth blocks 2π sr of the field of view, and changes between night and day take place very quickly, leading to breaks in visibility of the studied source about once every hour. Such an orbit was chosen for the Hubble telescope because it could be easily accessed by the space shuttle.

In *high circular orbit* (6 000 to 100 000 km), pointing is easier, observation periods are long, blocking of the field of view by the Earth is reduced, and interference from scattering, or

radiofrequency and thermal emissions, due to the Earth is weaker. On the other hand, the energy required for the launch and for communication is greater, and the costs are therefore higher. Such an orbit was chosen for the satellite Hipparcos (1989), but was never attained, owing to failure of a boost motor.

A compromise can be made by choosing a highly *elliptical orbit*, which requires less power for the launch, and passes close to the Earth to transmit its data, although this involves storing data on board; the satellite nevertheless spends most of its time far from the Earth and its associated interference emissions. The distance of the ISO satellite (Infrared Space Observatory, 1995), placed in an elliptical orbit, thus varied between 2 000 and 70 000 km.

The best orbits for γ ray astronomy are either very distant, avoiding the radiation belts, or else close circular equatorial orbits, avoiding the South Atlantic Anomaly and protected from cosmic rays by the magnetosphere. The latter offer by far the most suitable conditions for observation, but, unfortunately, are rather inaccessible from most of the larger launch pads (Cape Canaveral in Florida and Baikonour in Central Asia), and represent no interest whatsoever from the economic point of view (for telecommunications or remote sensing), or from a military point of view (observation of the Earth's surface). They are thus left unexploited by the space agencies. Indeed, there are some problems associated with them. Their occultation by the Earth limits observation periods and complicates manoeuvres. Radio links with the satellite are usually very short, unless a large number of relay satellites are available (a system of relay satellites called Transmission Data Relay Satellite System, TDRSS). In general, a mass memory must be installed aboard the satellite. For all these reasons, distant circular orbits ($>60\,000$ km), or eccentric orbits (apogee around 200 000 km), are considered to represent the best compromise; although there is more noise, observation and transmission conditions are less restrictive.

Finally, the *Lagrange points*¹⁴ should be mentioned. These are rather special locations in space at which the gravitational fields of the Earth and the Sun combine to give a local minimum of gravitational potential, thus favouring a stable orbit there. Given two bodies, there are five points at which a small object can remain in stable or unstable equilibrium while co-orbiting with the Earth (E) around the Sun: three are located on the line SE, L_1 (between S and E) and L_2 at 1.5×10^6 km symmetrically with respect to E, L_3 opposite E; L_4 and L_5 sit at the vertices of two symmetrical equilateral triangles with base SE. If a satellite is placed at one of these points, it can maintain a fixed position with respect to the Earth and the Sun, which is a great help for communications, but also for controlling thermal conditions. The European solar observatory SOHO (1995) occupies the point L_1 , while L_2 is or will be occupied by the European missions Planck (2008), Herschel (2008), and Gaia (2011), then NASA's JWST (2013), successor to the Hubble Space Telescope.

As yet, no observatory operating beyond the confines of the Solar System, and therefore outside the interference emissions of the Sun or the zodiacal nebula, has been seriously envisaged, for reasons of cost and owing to the problem of fast transmission to Earth.

2.10 The Moon as an Astronomical Site

The Moon was explored for the last time by the astronauts of the mission Apollo 17 in 1972, and completely surveyed by the unmanned probe Clementine in 1994. The density of the lunar atmosphere is a factor of 10^{14} less than that of the Earth at

¹⁴Named after the French mathematician Joseph-Louis Lagrange (1736–1813), originally from the Piemonte, author of the *Treatise on Analytical Mechanics*, which uses differential calculus. He proved the existence of the stable points in the Solar System which carry his name.

its surface, and the Moon can be considered to be practically without atmosphere. It thus offers observation conditions very similar to those encountered in interplanetary space, which give access to the whole of the electromagnetic spectrum.

We briefly discuss the main features of the Moon's surface that are relevant to setting up astronomical observatories:

- The lunar day lasts 27.321 terrestrial days. Such a long night allows long integration periods on a single source. In the polar craters, and in particular in the deep crater discovered at the south pole, the Sun only grazes the horizon, offering simultaneously a source of energy and a permanent state of half-night.
- The lunar surface is stable, seismic activity being less by a factor of 10^8 than on Earth. This could provide an almost infinitely stable foundation for telescopes. The stability would be invaluable for long baseline interferometry, which could extend over hectometres or kilometres, in the seas or in the depths of craters, and could observe at wavelengths anywhere from the ultraviolet to the millimetre range.
- The absolute instantaneous position of the Moon relative to stellar reference frames (see Chap. 4) is known to a very high degree of accuracy, far greater than the accuracy to which the position of an orbiting observatory can be known. The absolute position of the Moon, and its position relative to the Earth, are known to within a few millimetres, which is quite remarkable.
- The ground temperature varies widely between day and night, from 90 to 400 K except perhaps at high latitudes. This is a major disadvantage as regards thermal protection of instrumentation, but the very low temperatures reached by the ground provide a potential cryogenic source which would be invaluable for the cooling of telescopes, in the infrared and submillimetre regions, and for the cooling of detectors.
- The weak gravity on the Moon (0.16 g) makes it possible to build large structures which are both rigid and light. It is sufficiently strong, however, to bring surface dust back down to the ground, whereas any debris in space tends to co-orbit with its source. There nevertheless remains some uncertainty concerning the effects of a surface electric field on the dust; the surface of the dust grains is charged by the photoelectric effect of solar UV and by the space charge associated with it.
- The face of the Moon which remains permanently hidden from the Earth is entirely free of man-made radiofrequency interference, a fact which would strongly favour the setting up of radiotelescopes. Moreover, there is no ionosphere, and this would open the way to very low frequency radioastronomy, between 30 MHz and 100 kHz, which means wavelengths between 10 m and 30 km, a range quite inaccessible on the Earth, unless conditions are exceptional. Combination with a radiotelescope carried by satellite would then provide very long baseline observations, even at these frequencies. This part of the spectrum has hardly been explored as yet.
- Apart from the cost of setting up a lunar base, either manned or operated by robots, the main disadvantages are: the continual bombardment of the lunar surface by the solar wind and cosmic rays; the intense solar radiation in the EUV and X-ray regions; and the incessant impacts of micrometeorites (100 microcraters larger than 0.05 mm across are created per square metre per year).

Even though the construction of an astronomical base on the Moon is not for the immediate future, it is important to bear the idea in mind, because in some ways a lunar site could compete with orbital sites.

Problems

2.1. Using the fractional content of water vapour in air (Fig. 2.3), calculate the total quantity of precipitable water above the altitudes 4 km (Hawaii-sized mountain) and 12 km (airborne observatory).

2.2. The absorption cross-section of molecular oxygen is roughly $\kappa = 10^{-1} \text{ cm}^2 \text{ g}^{-1}$. Calculate the horizontal optical depth of the atmosphere over a length $l = 1 \text{ km}$ at altitude $z = 4 \text{ km}$, in the molecular oxygen absorption band at wavelength $\lambda = 4.8 \text{ mm}$ ($\nu = 62.5 \text{ GHz}$). Compare the result with the values given in Fig. 2.6. Calculate the integrated optical depth for the whole atmosphere.

Answer. The mass of O_2 along a horizontal line of length l , and per unit normal area, is

$$\frac{l \rho_0(z) M(\text{O}_2)}{5M_0},$$

where $\rho_0(z)/M_0$ is the molecular density at altitude z , and $M(\text{O}_2)$ is the molecular mass of O_2 . At $z = 4 \text{ km}$, $M_0 = 29 \text{ g}$ and

$$\rho_0(z) = e^{-z/H} M_0 \frac{P}{RT_0} = 774 \text{ g m}^{-3},$$

which gives $\tau = 10^3 \times 774 \times 32 \times 10^{-1} \times 10^{-4} / 29 \times 5 = 1.7$. This should be compared with the value given in Fig. 2.6; the attenuation in db km^{-1} is approximately 5, which implies $\tau = 5 \times 0.23 = 1.15$.

Vertically, the mass of O_2 per unit area normal to the vertical line is

$$\frac{M(\text{O}_2)}{5M_0} \int \rho_0(z) dz,$$

which implies that $\tau = 22.6$ from ground level, and $\tau = 13.6$ from $z = 4 \text{ km}$. The atmosphere is thus optically thick at this wavelength.

2.3. Find the damping coefficient γ for the pure rotational transition of the H_2O molecule at $\lambda = 2.1 \text{ mm}$, assuming that the band profile is Lorentzian (Fig. 2.6). Compare the value obtained with the collision frequency at the given pressure.

2.4. From the variation of horizontal attenuation of a band of O_2 as a function of altitude (Fig. 2.6), calculate the scale height of this component in the troposphere. Calculate the scale height of H_2O for the concentrations used in Fig. 2.6.

Answer. The z dependence of the horizontal attenuation A is

$$A(\text{O}_2) \propto \rho_{\text{O}_2}(z) \propto e^{-z/H},$$

which implies $H = (z_2 - z_1) / \log(A_1/A_2)$. Then, from Fig. 2.6, $H = 8 \text{ km}$ for O_2 and $H = 4.5 \text{ km}$ for H_2O .

2.5. What is the wavelength limit for near ultraviolet observations from a site at an altitude of $z = 2.86$ km (Pic du Midi observatory, France), or $z = 4.2$ km (Mauna Kea, Hawaii)?

2.6. Calculate the collision frequency of atmospheric constituents at an altitude of $z = 100$ km, and compare it with the frequency of spontaneous radiative decay of neutral oxygen O I by the transition 1S to 1D , with wavelength $\lambda = 557.5$ nm, for which $A_{\text{rad}} = 1.34 \text{ s}^{-1}$. Adopt a collision cross-section of $\sigma \approx 10^{-20} \text{ m}^2$.

Answer. For $z = 100$ km, $T = 210$ K and $P = 10^{-3}$ mb, and the typical speed v of a molecule is given by

$$\frac{3}{2}kT = \frac{M_0 \langle v^2 \rangle}{2N} \quad \text{implying} \quad v = \sqrt{\frac{3kTN}{M_0}},$$

where N is Avogadro's number. The typical molecular density is $n = PN/RT$, and the typical time between two collisions

$$t = A_{\text{col}}^{-1} \approx \frac{1}{n\sigma v} = 0.8 \text{ s},$$

implying $A_{\text{col}} = 1.2 \text{ s}^{-1} \gg A_{\text{rad}}$. At this altitude, the collisional de-excitation rate has decreased sufficiently for spontaneous radiative de-excitation to become significant.

2.7. At an astronomical site of average quality, the seeing disc of a star has an angular size of $2''$. At an exceptional site, and at the right moment, an optimised

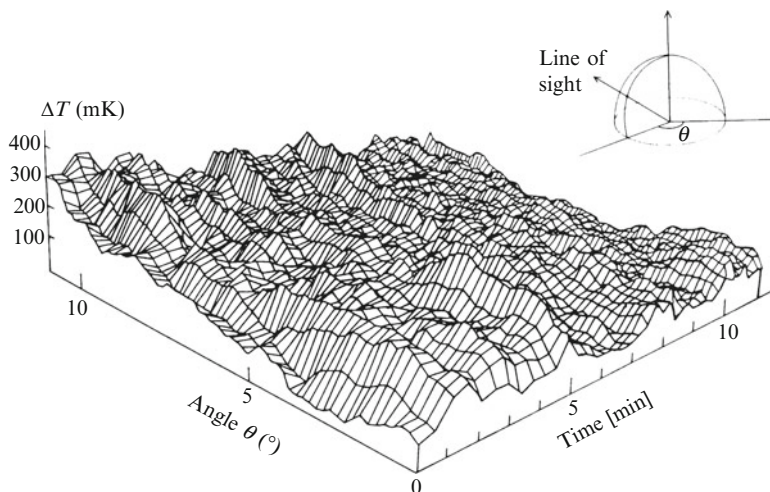


Fig. 2.25 Space and time fluctuations of the atmosphere at submillimetric wavelengths (Mauna Kea, Hawaii, 4 200 m)

telescope can give an image ten times smaller. What is the gain in contrast obtained for the detection of a quasar (angular size $\ll 1''$), or for the detection of a galaxy (angular size $> 1''$)?

Answer. The energy of an unresolved source (in this case, a quasar) is diluted in the marks it generates across the image plane. The gain in spatial resolution thus leads directly to a gain in contrast. On the other hand, for a resolved source, there is no effect whatsoever, the flux received per pixel being the same. Apart from improving image resolution, the techniques of *adaptive optics* can thus increase the capacity to detect weak unresolved sources.

2.8. Submillimetre Observations on Hawaii. The space and time fluctuations $I_\sigma(\theta, t)$ of atmospheric emission are measured at Mauna Kea, altitude $z = 4.2$ km, $\sigma = 11 \text{ cm}^{-1}$, where θ is the azimuth of the line of site and t the time. Rayleigh–Jeans emission is assumed, with brightness temperature $\langle T \rangle = 100$ K. Figure 2.25 shows the fluctuation ΔT (mK) (ordinate) for this brightness temperature. From the figure, estimate the mean emissivity ε of the atmosphere, and also the standard deviations σ_θ and σ_t , in space and time, respectively, of the received emission. Given that the average wind speed is $v = 35 \text{ km hr}^{-1}$ during these measurements, calculate the average size of the atmospheric inhomogeneities causing the observed fluctuations. (After Pajot F., Thesis, 1983.)

Observational Astrophysics

Léna, P.; Rouan, D.; Lebrun, F.; Mignard, F.; Pelat, D.

2012, XV, 719 p. 128 illus., 71 illus. in color., Hardcover

ISBN: 978-3-642-21814-9